Metallurgy and Foundry Engineering – Vol. 41, 2015, No. 1, pp. 17–28
http://dx.doi.org/10.7494/mafe.2015.41.1.17

Piotr Migas, Marta Ślęzak

High-temperature rheometry of blast furnace synthetic slags doped with TiO_2 and TiN

Wysokotemperaturowe badania reometryczne wielkopiecowych żużli syntetycznych domieszkowanych TiO_2 oraz TiN

Abstract

Development has been conducted regarding the methodology of rotational measurements with a high temperature rheometer using Searle's method. The rheological analysis of liquid systems $CaO\text{-}SiO_2\text{-}Al_2O_3\text{-}MgO\text{-}TiO_2$ slags, and solid particles of titanium nitride TiN are presented (within a range of 0.1–0.7 of the volume fraction of TiN). The measurements were conducted at a range between 1310°C and 1500°C, which is typical for high-temperature zones in a blast furnace. The main objective of the study was to analyze the possibilities of viscosity measurements in homogenise and heterogenic systems (not standard systems within the industrial practice). The measurements were conducted for totally liquid blast furnace slags which show similarity to ideally viscous Newtonian bodies and also for heterogenic systems.

Keywords: slag viscosity, high-temperature rheometry, titanium nitride, rheology

Streszczenie

W pracy zaprezentowano wyniki badań przeprowadzonych z wykorzystaniem reometrii wysokotemperaturowej opartej na metodzie Searle'a. Przeprowadzono analizę reologiczną ciekłych systemów żużlowych $CaO\text{-}SiO_2\text{-}Al_2O_3\text{-}MgO\text{-}TiO_2$ domieszkowanych TiN, w zakresie 0,1–0,7 ułamka objętościowego. Badania przeprowadzono w temperaturze 1310–1500°C, która jest charakterystyczna dla strefy ściekania występującej w wielkim piecu. Głównym celem prowadzonych badań była analiza reologiczna współczynnika lepkości dynamicznej oraz możliwości wysokotemperaturowych pomiarów reometrycznych układów homo- oraz heterogenicznych (rozszerzających zakresy przemysłowe). Badania przeprowadzono zarówno dla parametrów reologicznych dla całkowicie ciekłych systemów żużlowych, które wykazują podobieństwo do cieczy idealnej Newtona, jak i dla układów heterogenicznych.

Słowa kluczowe: lepkość żużla, reometria wysokotemperaturowa, azotek tytanu, reologia

Piotr Migas Ph.D. Eng., Marta Ślęzak Ph.D. Eng.: AGH University of Science and Technology, Faculty of Metals Engineering and Industrial Computer Science; Krakow, Poland; e-mail: pmigas@agh.edu.pl

1. Introduction

Two non-mixing liquid phases are involved in the blast furnace process. These are liquid iron and liquid tapping silicate melts – along with metal oxides – which do not get reduced in a blast furnace at all (or only to a limited degree).

Blast furnace slag significantly influences the course of the thermo-chemical effects in the process of obtaining iron. It is an important factor in regards to the right mechanics of charge material movement in a blast furnace and the correct flow of reducing gases through the charge mass [1–3].

The addition of TiO_2 to the system decreases its dynamic viscosity by depolymerization of the network structure. Results of an XPS analysis show that the bridged oxygen (O^0) content declines with the addition of TiO_2, while the free oxygen content (O^{2-}) increases. The addition of over 5% TiO_2 to the system (with constant basicity $B_1 = 0.8$) has a comparably lesser effect on the share of the fraction O^0, O^-, and O^{2-}, which appears to correlate well with the results of viscosity measurements. It seems that an increase in basicity will be more significant for viscosity reduction than the addition of TiO_2 [4, 5].

The different authors [6–9] analyzed the viscosity of various slag grades; however, none of the known and applied theories of slag structure satisfactorily describe the influence of TiO_2 on the structure of liquid silicates. The main reason for this is the fact that these theories have been developed in order to identify the physical properties of liquid silicate systems. However, the viscosity values and their changes with temperature changes for high concentrations of TiO_2 in the system differ significantly from those values and changes for typical polymerised silicate liquids. This proves that slags with an addition of TiO_2 have a substantially different structure [8]. It seems that this opinion is still valid, having arisen from the heterogeneous structure of the systems analyzed and the participation of solids in the system.

Continuous work and research [1–18] enable to apprize the influence of the addition of titanium compounds to a blast furnace on the ironmaking process and the hearth carbon refractory lining to be determined.

2. Research approches

Rheometric measurements of semi-solid slag systems of the blast-furnace type were performed within a temperature range of 1310–1500°C in an inert-reduction atmosphere. The base slag (sample 1-basis) with the chemical composition as presented in Table 1 had the addition of rutile-TiO_2 within a range of 0.5–3% by weight and within a range of 6–30% TiO_2. Solid TiN was also added, which was treated as a substance that had precipitated from the system.

The authors [14, 15] examined the possibilities of precipitation of titanium compounds from blast furnace slags with the addition of TiO_2. On the basis of the chemical

stability of minerals, they found that within a temperature range of 1450–1100°C, titanium compounds precipitate in the following sequence: Ti(N,C), perovskite, spinel (Al_2O_3·MgO), Ti-rich diopside, and Ti-bearing diopside. The experimental results show that – apart from titanium carbonitrides – the perovskite phase is one of the first phases precipitating [15].

Table 1. Chemical compositions of the analyzed slag systems

Sample description	CaO	MgO	Al_2O_3	SiO_2	TiO_2	TiN
	[%]					
1 – basis	43.71	7.97	8.50	39.10	0.00	–
2 – low concentr. TiO_2	43.29	8.39	8.52	38.68	0.48	–
3 – low concentr. TiO_2	42.96	8.35	8.56	38.13	1.45	–
4 – low concentr. TiO_2	42.43	8.04	8.50	37.62	2.87	–
5 – high concentr TiO_2	42.54	7.22	9.86	32.98	5.81	–
6 – high concentr TiO_2	28.95	7.62	9.10	24.31	29.73	–
7 – TiN (min. 5.81% TiO_2)	1-basis + TiN					3.44
8 – TiN (max 5.81% TiO_2)	1-basis + TiN					4.14
9 – TiN (min. 29.73% TiO_2)	1-basis + TiN					17.67
10 – TiN (max 1.45% TiO_2)	1-basis + TiN					21.58
11 – TiN (max 2.87% TiO_2)	1-basis + TiN					1.67

The shape and size of perovskite precipitates change depending on temperature (1300°C or 1370°C), chemical composition, and rate of cooling. Crystals of pervoskites are dendrites – long, not round; thus, they might have an influence on the rheological character of the system [15].

Due to the presence of solid particles in the systems (in the conditions of rheological experiments), a theoretical analysis of solids was performed. The amount of TiN particles in the system was calculated with the FactSage thermodynamic database – equilibrium module. Within the assumed conditions of temperatures, compositions, and pressures of gases (N_2 and CO), possible theoretical quantities of TiN precipitates in the equilibrium state were calculated. High temperature rheometrical measurements were performed for these conditions: these were for chemical compositions of slag doped with 1.45%, 2.87%, 5.81%, and 29.73% TiO_2 respectively in a sample of 50 g of the slag.

A high temperature FRS 1600 rheometer was used for the measurements, with the measuring systems presented in publications [12, 13].

Synthetic slags were prepared from chemical-reacting substances from the Merck and Aldrich companies. Pure oxides were melted to be synthesized under an inert atmosphere (5.0 Ar purity) at a temperature of 1500°C. This slag formed the base which subsequently was doped with TiO_2 and TiN. Solid particles did not exceed 3 μm and therefore remained unchanged. Chemical compositions of the slag systems that were analyzed are presented in Table 1. The analysis was performed with an XRF Twin-X spectrometer.

Samples 5 and 6 correspond to the possible theoretical amount of precipitated TiN (for 5.81% TiO_2). These values were calculated for two cases, based on the minimum and maximum amount of TiN and dependant on the pressures and concentrations of N_2, CO within the furnace tube. The samples 8 – 29.73% TiO_2, 10 – 1.44% TiO_2, and 11 – 2.87% TiO_2, correspond only to the maximum theoretical amount of TiN that was obtained by reduction and precipitation under specific conditions of pressure, temperature, and chemical composition.

3. Analysis of findings

High temperatures rheometry measurements have been performed, and additionally, an SEM analysis in a micro-area for the selected samples also has been done. Sample 1 – containing 5.81% TiO_2 – is presented in Figure 1. The analysis was performed at the liquid-crucible interface. High concentrations of titanium as well as carbon and nitrogen can be observed; titanium most likely occurs in the forms of TiC, Ti(C,N), and TiN. This confirms the hypothesis in that the titanium compounds are formed as a result of the reaction of carbon and nitrogen that are present in the system. These titanium compounds are solid within the specific conditions of the experiment, and affect the dynamic viscosity coefficient of the liquid. At high temperatures, titanium oxide may be reduced from the slag-liquid phase with the crucible carbon, and titanium carbonitrides may precipitate [12, 15] (Fig. 1). However, at lower temperatures, the perovskite phase may precipitate [15] (apart from the existing high-melting solid particles).

Figure 2 presents the flow curves for the base slag without the addition of titanium compounds. It can be concluded from the curves that the analyzed system shows similarities to a Newtonian viscous liquid.

X.L. Tang et al. [16] reported measurements that were carried out at five different speeds of rotation, varying from 100 to 200 rpm at each temperature. The variation of viscosity values (due to the variable rotation speeds) is less than 2%, indicating that the melt behaves like a Newtonian liquid. However, the systems analyzed were CaO-SiO_2-Al_2O_3-MgO with different alumina concentrations of 5–20% [18].

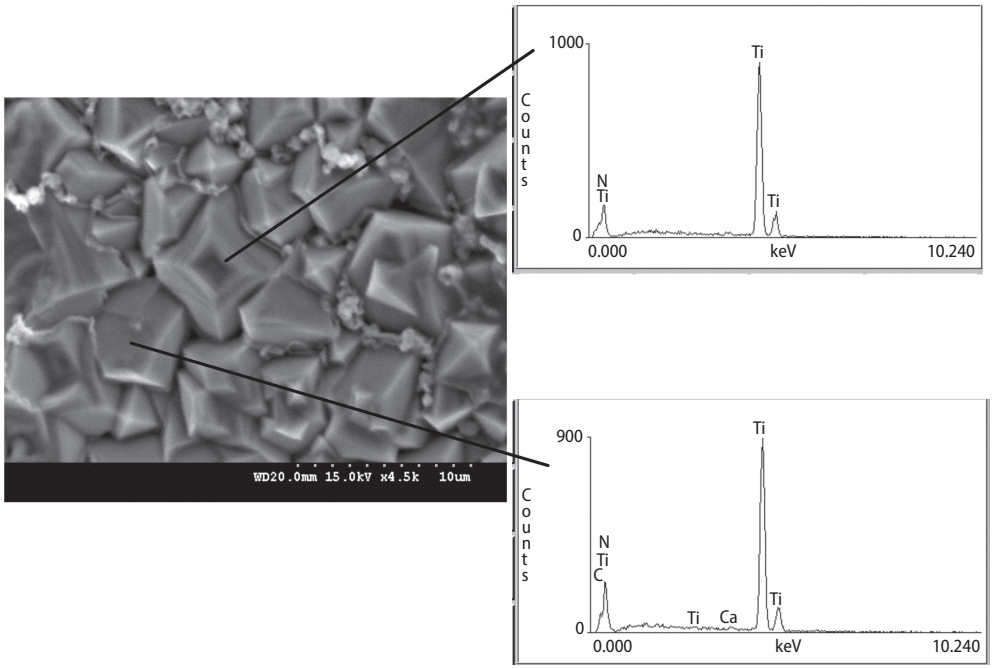

Fig. 1. SEM for sample 5 – high concentration of TiO_2

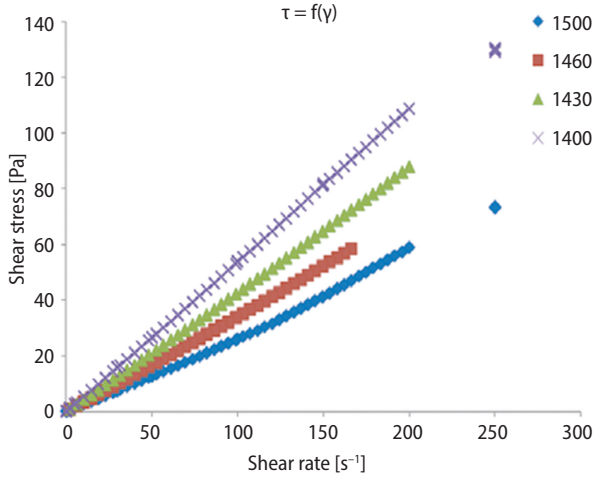

Fig. 2. Flow curves for the basic blast furnace slag samples

The authors of this study have also applied the FactSage thermodynamic database to calculate the possibility of TiO_2 reduction in the particular conditions of a state of equilibrium. One can find that titanium oxide in the analyzed conditions will be slightly

reduced to lower oxides, and when the temperature decreases, solid particles will precipitate in the form of perovskite, TiN, and Ti(C,N). Based on the observations taken after the rheometric tests of the measurement tools (cup, bob), no changes in the linear dimensions of those tools in the area of cup-slag or bob-slag contact were observed. Significant changes in the linear dimensions could influence the rheometric measurement results.

In order to calculate the activation energy for viscous flow (E_η), the Arrhenius type relationship of equation (1) was used, and the slope from the plot of the natural logarithm of the viscosity (ln η) with reciprocal temperature (1/T) provided E_η [4].

$$\eta = \eta_0 \exp\left(\frac{E_\eta}{RT}\right) \tag{1}$$

Table 2 shows the calculated [4] activation energies for the various slag compositions, where values between 195 to 262 kJ/mol were calculated depending on the various slag compositions. These values are comparable to the results obtained by others authors between 150 to 210 kJ/mol for CaO-SiO_2-20% mass Al_2O_3 slags at constant CaO/SiO_2 of unity and containing either MgO or TiO_2 and published activation energy values of viscous flow from 200 to 240 kJ/mol for the CaO-SiO_2-20% mass Al_2O_3-10% mass MgO slags at CaO/SiO_2 from 0.8 to 1.2, which is also comparable to study of Sohn et al. [4].

Table 2. Calculated activation energy [4]

CaO/SiO_2	**TiO_2**		
	0% mass	**5% mass**	**10% mass**
	Activation energy Eη [kJ/mol]		
0.8	206 ± 3	221 ± 7	195 ± 4
1.0	220± 7	199 ± 12	209 ± 18
1.2	225 ± 9	246 ± 1	262 ± 4

The authors of this study have performed rheometric measurements of a comparable slag system of CaO-SiO_2-Al_2O_3-MgO with TiO_2 additions. The values of activation energy for TiO_2 concentrations within the range of 0.5–3% TiO_2 were calculated based on the results of dynamic viscosity coefficient obtained by the authors.

Equation (2), determining the slag basicity under the molecular theory [17], was applied to calculate the hypothetical value of the dynamic viscosity coefficient for the shear rate approaching zero.

$$B = \frac{CaO + MgO + K_2O + Na_2O}{SiO_2 + Al_2O_3 + TiO_2} \tag{2}$$

Next, the relationship of the dynamic viscosity coefficient η_0 as a function of system basicity – B – was plotted. The graph is presented in Figure 3. For samples 1, 2, 3, and 4, value η_0 was determined.

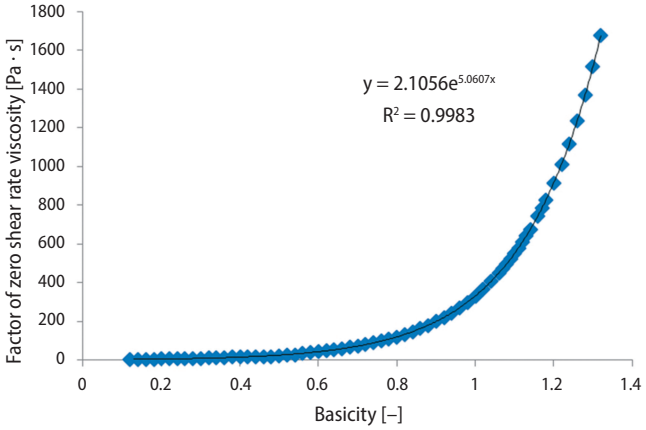

Fig. 3. Viscosity $\eta_0 = f(B)$

The viscous flow activation energy values were calculated based on the Arhenius–Guzmann's equation (1) and the rheometric measurement results. The findings are presented in Figure 4.

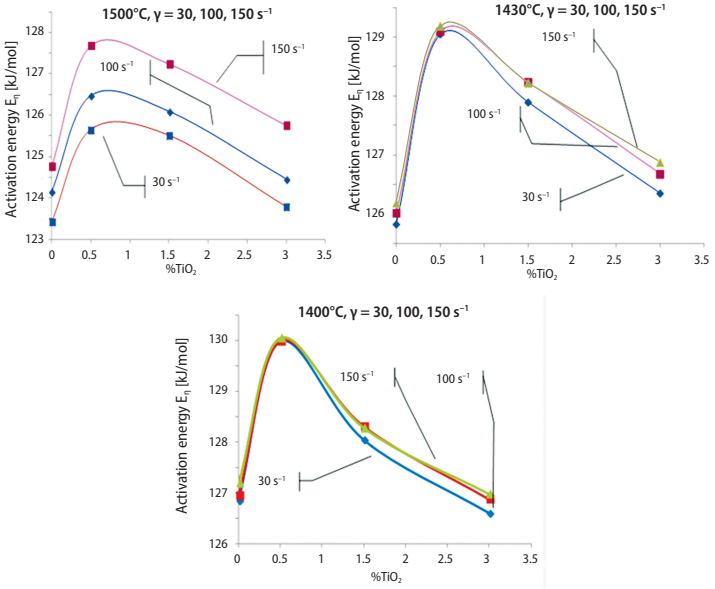

Fig. 4. Calculated activation energy for different temperatures and shear rates

Changes of the activation energy values – which show a non-linear nature – can be seen in Figure 5. The values of activation energy depend not only on temperature values but also on shear rate values. For all temperatures analyzed, deviations from a straight line could be observed. It seems that the formation and precipitation of solid particles at these temperatures – carbonitrides, titanium oxides, perovskite, and others – do imply those deviations that were observed. Deviations from a straight line may also result from a change in the internal structure of the liquid remaining in the system; i.e., its polymerisation. It is similar to the case of the tests conducted by the authors [18]. An increase in viscous flow activation energy for a decreasing temperature can be observed. At high temperatures of 1500°C, a considerable influence of shear rate on the activation energy value can also be observed, while its changes maintain a similar nature. At a shear rate of 150 s^{-1}, the energy activation value is at its maximum. Also, the influence of TiO_2 concentration on the activation energy level can be observed. In each case, the energy is at its maximum for a concentration of 0.5% TiO_2, and it subsequently decreases as the TiO_2 content in the system increases. It indicates a significant influence of TiO_2 on the depolymerization of the internal structure of the whole system.

Figure 5 presents a change in the viscous flow activation energy depending on the TiO_2 concentration in slag. For liquids in which a constant change in structure occurs at a specific temperature (e.g., polymerisation or depolymerization), a change in the activation energy should be rectilinear. A change in the activation energy as a function of TiO_2 and Ti_2O_3 concentration is non-linear. Also, the Ti_2O_3 content more effectively reduces E_η than TiO_2.

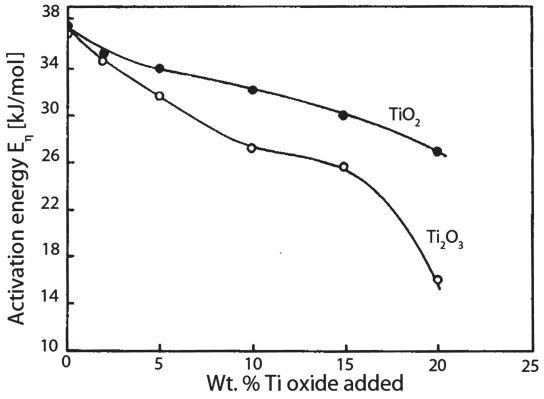

Fig. 5. Change in the activation energy as a function of TiO_2 addition to slag [17]

For the addition of 20% Ti_2O_3, the activation energy falls by ca. 57% when compared to the initial value, whereas for TiO_2, this energy drop is about 27%. Both curves have irregular shapes Authors [17] have obtained similar irregularities for the same type of slag). Slags of this type do not meet the Arrhenius dependency, which may reflect

a continuous change in their internal structure as the temperature changes. The precipitation of finely dispersed solid particles in the slag volume is another possibility, which changes the nature of the flow and the nature of the liquid. For up to 10% TiO_2 in slag, its viscosity declines whereas fusibility drastically increases (there is a rise in the melting temperature), thus causing an increase in fluidity/castability [17].

By comparing both Figures 4 and 5, it can be observed that the nature of changes in the activation energy values is different, while these values are comparable. The authors [17] have obtained activation energy values between 26 and 37 kcal/mol for TiO_2 concentrations from 0% to 20% whereas, in this study, activation energy varies from 29 to 31 kcal/mol for TiO_2 concentrations from 0% to 3%. The values of activation energy for comparable slag systems (presented in Table 2) are almost twice the amount as those obtained in this study, and may be a result of a slightly different slag system that was analyzed. The kind of material used for the measurement tools could modify the energy value to a small extent. In the following study, the measurement systems/tools were made of graphite; therefore, the authors have obtained an inert-reducing atmosphere that is comparable to the atmosphere of a blast furnace in terms of quality. The biggest influence of shear rate on the activation energy value is observed at a temperature of 1500°C (where the reaction of TiO_2 reduction is most likely to be the most intensive), thus changing the internal structure of a wholly liquid system. The lowest energy value occurs exactly for this case (1500°C), and this can be identified as the depolymerizing impact of TiO_2 on the lattice structure of liquid silicates. For lower temperatures (1430°C, 1400°C), higher energy values were obtained: these were not as diverse in terms of the change nature and can be substantiated by the precipitation of solids in the system, along with changes in the lattice structure that were not so significant. Similar deviations are illustrated in Figure 5.

Figures 6a,b present changes in the viscosity coefficient values as a function of TiO_2 concentration (for samples 2, 3, and 4) and TiN concentration (for samples 5, 6, 10, and 11) at temperatures of 1500°C and 1460°C. For the presence of TiO_2 in the system, a slight influence of shear rate on the viscosity value can be seen. The values of viscosity coefficients change depending on the TiO_2 share and the shear rate within these ranges.

It can also be observed that an increasing number of solids in the liquid slag causes an increase in the viscosity coefficient of the whole system. In addition, a significant impact of the shear rate appears.

Viscosity coefficients for the selected samples 4 (TiO_2) and 11 (TiN) are compared in Figure 7. It can be observed that the viscosities for a system with the theoretical TiN content corresponding to the TiO_2 amount that reacted with nitrogen are not comparable. The viscosities for the system with TiN, for the temperatures of 1490°C and 1340°C, are much higher, and the system rheological character is changed.

The theoretically calculated amounts of TiN that may precipitate from the system at a given TiO_2 content – according to the obtained rheometric results (the values of viscosity coefficients) – are too excessive for the specific thermodynamic conditions. For the

system analyzed, the viscosity values should be comparable at a given constant temperature of 1490°C (for samples 4 and 11) and 1340°C (for samples 4 and 11).

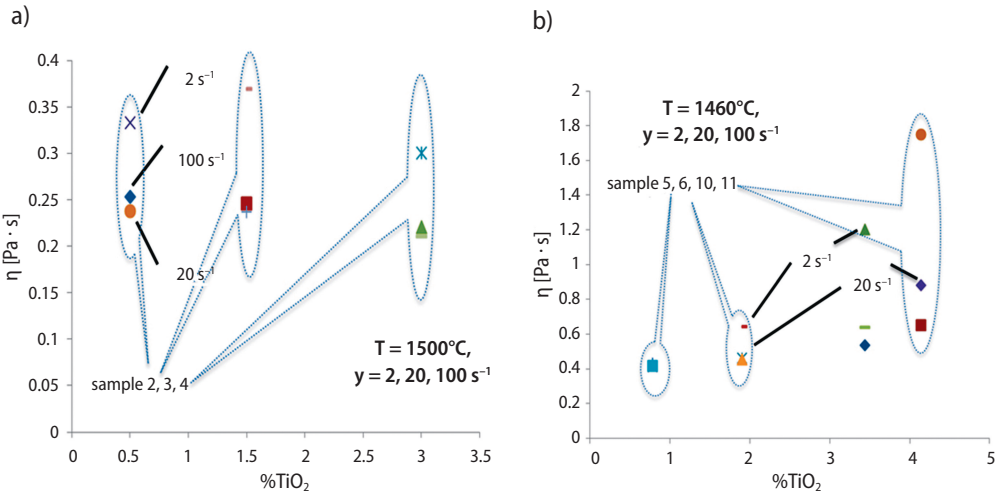

Fig. 6. Change in the viscosity coefficient versus: a) TiO_2; b) TiN

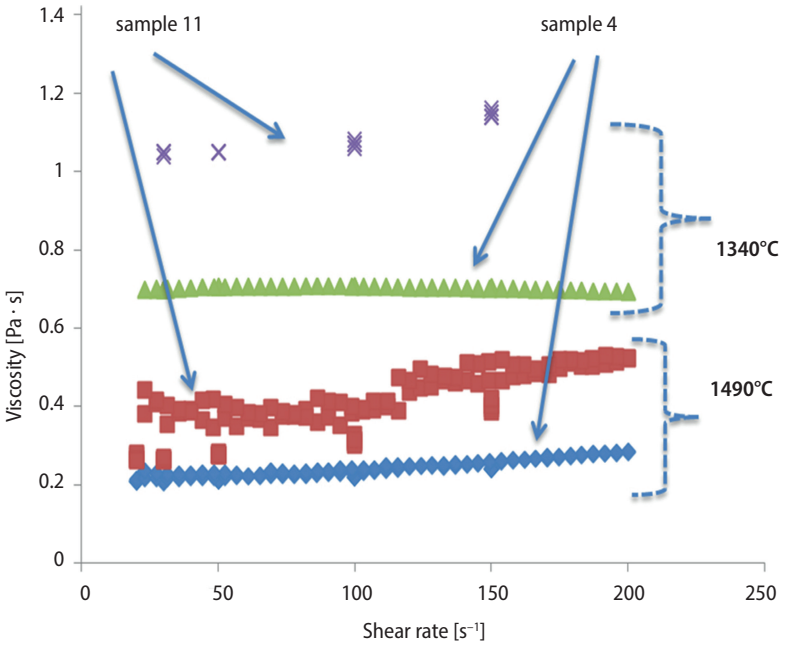

Fig. 7. Differences in the component (sample 4 – TiO_2 and sample 11 – TiN) influence on viscosity

4. Conclusions

Based on the performed rheometric tests, one can find that the analyzed four-component blast furnace slag CaO-SiO_2-MgO-Al_2O_3 shows similarities to Newtonian viscous liquid within a temperature range of 1400–1500°C, and a shear rate of 2–200 s^{-1}.

1) The addition of 0,48–2,87% TiO_2 to the blast furnace slag causes a decline in the dynamic viscosity coefficient value for low shear rates 2 s^{-1}.
2) For higher shear rates (20, 100 s^{-1}), the viscosity drop is insignificant. However, when TiN is added to the system, the opposite occurs in the behavior of the system, the viscosity growing with an increase in shear rate.
3) The conducted research has confirmed the effect of TiO_2, which, due to its nature, may be considered a network modifier, reducing the viscosity of the whole system.
4) The greater share of solids (TiN) in the system, the higher value of the viscosity coefficient. For low TiO_2 concentrations and adequate (comparable) TiN contents, the rheological nature of the liquid changes from a Newtonian system to a slightly shear-thinning system.
   It seems necessary to conduct further work on the behavior of the solid-liquid rheological slag systems. The flow nature of the analyzed heterogenic systems is very important from the point of view of liquid behavior phenomena: stick and flowing through the coke bed in a blast furnace.

Acknowledgements

Financial support of National Science Center for the research project "Developing an empirical model of the rheological properties of liquid metals on the example of iron solutions" No. 2011/01/N/ST8/07368 is gratefully acknowledged.

The research was conducted with the financial support from statutory project No. 11.11.110.225.

References

[1] Hartig W., Amirzadeh-Asl D., Fünders D.: Use of Synthetic Titanium Products for Protection of the Hearth of Rogesa Blast Furnaces. XXXVII Ironmaking and Raw Materials Seminar, Salvador, MG, Brazil, September 18–21, 2007

[2] Kurunov I.F., Loginov V.N., Tikhonov D.N.: Methods of Extending a Blast-Furnace Campaign. Metallurgist, 50 (2006), 605–613

[3] Dierich J.-Ch., Bauer W., Amirzadeh-Asl D., Fünders D.: Synthetic Titanium in Blast Furnaces. http://www.sachtleben.de, 2014

[4] Sohn I., Wang W., Matsuura H., Tsukihashi F., Min D.J.: Influence of TiO_2 on the Viscous Behavior of Calcium Silicate Melts Containing 17 Mass% Al_2O_3 and 10 Mass% MgO. ISIJ International, 52 (2012), 158–160

[5] Zhang S., Zhang X., Bai Ch., Wen L., Lv X.: Effect of TiO_2 Content on the Structure of CaO-SiO_2-TiO_2 System by Molecular Dynamics Simulation. ISIJ International, 53 (2013), 1131–1137

[6] Li J., Zhang Z., Liu L., Wang W., Wang X.: Influence of Basicity and TiO_2, Content on the Precipitation Behavior of the Ti-Bearing Blast Furnace Slags. ISIJ International, 53 (2013), 1696–1703
[7] Zhang L., Jahanshahi S.: Modelling Viscosity of TiOx Containing Silicate Melts. VII International Conference on Molten Slags Fluxes and Salts, The South African Institute of Mining and Metallurgy, 2004, 51–56
[8] Handfield G., Charette G.G.: Viscosity and Structure of Industrial High TiO_2 Slags. Canadian Metallurgical Quarterly, 10 (1971), 235–243
[9] Handfield G., Charette G.G., Lee H.Y.: Viscosity of Industrial Titania Slags. "100th Aime Annual Meeting", Aluminum Company of Canada, Montreal, Canada, Proceedings Of Symposia, "Light Metals-1971", March 1–4, 1971
[10] Xie D., Mao Y., Zhu Y.: Viscosity and Flow Behaviour of TiO_2-Containing Blast Furnace Slags Under Reducing Conditions. VII International Conference on Molten Slags Fluxes and Salts, The South African Institute of Mining and Metallurgy, 2004
[11] Nakamoto M., Lee J., Tanaka T.: A Model for Estimation of Viscosity of Molten Silicate Slag. ISIJ International, 45 (2005), 651–656
[12] Migas P., Korolczuk-Hejnak M.: Rheology of blast furnace slags admitted high concentration of titanium oxides. Key Engineering Materials, 554–557 (2013), 536–546
[13] Korolczuk-Hejnak M., Migas P.: Selected grades of steel as rheologically defined liquid bodies. Archives of Metallurgy and Materials, 57 (2012), 583–591
[14] Morizane Y., Ozturk B., Fruehan R.J.: Thermodynamics of TiO_x in Blast Furnace-Type Slags. Metallurgical and Materials Transactions B, 30 (1999), 29–43
[15] Guo Z.Z., Lou T.P., Zhang L., Zhang L.N., Sui Z.T.: Precipitation and Growth of Perovskite Phase in Titanium Bearing Blast Furnace Slag. Acta Metallurgica Sinica (English Letters), 20 (2007), 9–14
[16] Long T.X., Zuo-Tai Z., Min G., Mei Z., Xi-Dong W.: Viscosities Behavior of CaO-$Si0_2$-MgO-Al_2O_3 Slag with Low Mass Ratio of CaO to SiO, and Wide Range of Al_2O_3 Content. Journal of Iron and Steel Research International, 18, 2 (2011), 1–6
[17] Williamson J., Wigley F. (eds): The Impact of Ash Deposition on Coal Fired Plants. Proceedings of the Engineering Foundation Conference, 1993
[18] Handfield G., Charette G.G., Lee H.Y.: Titanium Bearing Ore and Blast Furnace Slag Viscosity. Reprinted from Journal of Metals, September 1972

Metallurgy and Foundry Engineering – Vol. 41, 2015, No. 1, pp. 29–44
http://dx.doi.org/10.7494/mafe.2015.41.1.29

Paweł Hyjek, Iwona Sulima, Piotr Malczewski

Mechanical properties and corrosion resistance of cast NiAl alloys with the addition of Ti

Własności mechaniczne oraz odporność na korozję stopów NiAl z dodatkiem tytanu

Abstract
Results of compression- and corrosion-resistance tests of NiAl alloys with 1.0 and 2.0 wt.% of titanium are described. The compression tests conducted at a wide range of temperatures, and the strain rate showed that an increase in titanium content causes increased brittleness at room temperature, while at higher temperatures, an increase of hardness and strength is observed. The analysis of electrochemical corrosion resistance showed that alloys containing Ti are characterized by considerable resistance to sulfuric acid VI, because the emerging titanium oxide prevents the active solubilization of the alloy. Besides, microstructure observations performed at various levels of deformation, which allowed us to identify the mechanisms responsible for fracture of the studied alloys.

Keywords: NiAl alloys, compression, corrosion resistance

Streszczenie
W artykule zamieszczono wyniki badań wytrzymałości i odporności na korozję stopów na osnowie fazy NiAl z dodatkiem 1.0 i 2.0% wag. tytanu. Prowadzone w szerokim zakresie temperatur i prędkości odkształcania próby ściskania wykazały, że wzrost zawartości tytanu wpływa na zwiększenie kruchości stopu w temperaturze pokojowej, podczas gdy w podwyższonych temperaturach obserwuje się zwiększenie twardości i wytrzymałości. Analiza odporności na korozję elektrochemiczną ujawniła, że stopy zawierające tytan charakteryzują się znaczą odpornością na działanie kwasu siarkowego VI, bowiem powstający tlenek tytanu utrudnia aktywne roztwarzanie stopu. Wykonano także obserwacje mikrostrukturalne na różnych poziomach odkształcenia, które pozwoliły na identyfikację mechanizmów odpowiedzialnych za zniszczenie (pękanie) stopów.

Słowa kluczowe: stopy NiAl, ściskanie, odporność korozyjna

Paweł Hyjek Ph.D. Eng., Iwona Sulima Ph.D. Eng., Piotr Malczewski Ph.D. Eng.: Institute of Technology, Pedagogical University of Cracow; phyjek@up.krakow.pl

1. Introduction

Due to outstanding physic-chemical and mechanical properties, alloys with a matrix made of intermetallic phases containing aluminum belong to a group of materials operating at higher temperatures in a corrosive environment. Unique features of NiAl-based alloys include: low density, high melting temperature, good hardness, Young modulus and thermal conductivity as well as sufficient corrosion resistance. This choice of properties makes these alloys suitable for elements of gas turbines, combustion engines, heat exchangers and engines working at high temperatures and in a corrosive environment. The range of applications of these alloys is limited by insufficient ductility and resistance to cracking at ambient temperatures, as well as by their poor resistance to cracking at higher temperatures [1–5].

In order to extend the spectrum of applications of NiAl matrix alloys, studies regarding the improvement of mechanical properties are undertaken, mainly an increase of plasticity at room temperature by micro and macro alloying additions [3–6]. It was observed that, in the case of a single phase NiAl alloy with a B2 phase, there is a possibility of a significant control of brittleness. The generation of monocrystalline or fine policrystalline phase considerably increased ductility at higher temperatures. Still, attempts have been made towards decreasing brittleness at room temperature.

Until now, it has been shown that the addition of Cu, Fe, Ag, Co and Ti [7, 8] in the form of modifiers of single or binary phase structure significantly improves the mechanical properties of the intermetallic NiAl phase. Another solution for increasing the strength of NiAl alloys is the introduction of hard, fine ceramic particles that are metallurgically stable at higher temperatures [6, 9, 10].

Simultaneously to studies regarding mechanical properties of NiAl-based alloys, investigations were conducting towards determining corrosion resistance. The basic method of studying electrochemical properties of metals and alloys (passivation) is the determination of anodic or cathodic polarization curves. The dependence of density on an external polarization current flowing thorough a sample of potential U is measured at potentiostat with respect to a reference electrode. The obtained characteristics allow us to determine anodic behavior of a given alloy in certain environments. Besides, it is also possible to prepare and hold an alloy in a passive state as well as determine the influence of temperature and environment changes on a course of electrode processes and influence of corrosion inhibitors [11]. The advancing chemical or electrochemical corrosion may cause a considerable decrease of mechanical and tribological properties as well as economic losses due to damage to the materials.

It is to note that, in metallic alloys, structural parameters other than electrochemical ones strongly affect the intensity of corrosion. A condition for intensive electrochemical corrosion in alloys is the formation of galvanic microcells caused by the presence of at least two phases in the microstructure. Thus, the basic elements of microcells are secondary precipitates or metallic impurities present in a matrix (mainly at grain boundaries).

Moreover, energetic parameters connected with grain-size and internal stresses influence the intensity of the electrochemical corrosion; usually, the smaller the grain, the less corrosion. Although, many things were achieved in the understanding and description of this type of destruction process of metals and alloys, many experiments are still required [12].

2. Materials and experimental method

2.1. Obtaining alloys

Smelting techniques of intermetallic phases include: smelting in an open-induction furnace, smelting in a vacuum, induction remelting in a vacuum, and smelting in an arc furnace. The smelting process of intermetallic phase NiAl must be carried out under specific conditions due to the large difference in melting temperatures of pure aluminum (933 K) and nickel (1728 K), and the presence of an exothermic reaction occurring during synthesis (which is not insignificant for the metallurgic process). Due to the rapid increase in temperature immediately after an exothermic reaction, oxidation of aluminum in air takes place, which causes the formation of slag. Thus, precise control of an alloy's composition is rendered difficult.

The alloys for studies were produced in the Exomelt cost-saving process in a protective argon atmosphere at subatmospheric pressure of 0.5 MPa. The procedure of placing a charge material in equipment is described in [13]. The time necessary for reaching a pouring temperature was 500 s. For comparison, in a classic method, the time for reaching the melting temperature of pure nickel (when aluminum could be added) is 820 s. Therefore, saving of energy in the case of the modified Exomelt technique is 40%. The exothermic reaction of Ni-Al lasts a few seconds; then, the alloy can be poured by classic methods to a heated mould. The described method was applied for receiving NiAl with Ti and B additions. Boron was added in the form of master alloy Al-3%B after the exothermic reaction was finished.

The obtained alloys were poured to a multiple mould in an argon atmosphere, allowing for the receipt of four ingots with different dimensions depending on the destination of the samples. From the obtained rods, samples were cut by a spark-erosion cutting device for compression and Vickers hardness tests, and a series of specimens were cut for corrosion-resistance experiments.

2.2. Experimental methods

In order to control chemical and phase composition, alloys were subjected to X-ray analysis by a DRON-s diffractometer equipped with a copper tube with an LiF monochromator. Measurements were performed for 2θ in the range 20–120° at an exposure time of 6 s and a step size of 0.02°. The working voltage and current of the diffractometer were 42 kV and 18 mA, respectively.

Mechanical properties of NiAlTiB (A and B), where A and B correspond to various amounts of alloying additions, were evaluated on the basis of a compression test conducted at a wide range of temperatures and strain rates. The tests were carried out by an Instron universal machine equipped with a furnace with a dynamic-flow argon atmosphere. Samples with a diameter of 6 ± 0.03 mm and a height of 9 ± 0.05 mm were deformed at temperatures of 297, 673, 873, and 1073 K, with strain rates of $9.25 \cdot 10^{-5}\,s^{-1}$, $1.85 \cdot 10^{-4}\,s^{-1}$, and $1.85 \cdot 10^{-3}\,s^{-1}$. Prior to a test, the furnace temperature was stabilized at the required level, and each sample was held for 5 minutes before the test began to assure that there was no temperature gradient across the specimen.

Dependencies based on the concept of initial deformation proposed by Krupkowski [14] or Swift, or dependence based on the initial stress proposed by Ludwig ($\sigma = \sigma_o + Ke^n$) and modified by Hollomon ($\sigma = Ke^n$) and later by Ludwigson ($\sigma = Ke^n \pm \Delta$) are most often applied to the description of the deformation characteristics (σ-ε) [15]. It was observed in many metals and alloys that the characteristics (σ-ε) in double-logarythmic co-ordinate system $\log\sigma = f(\log\varepsilon)$ shows deviations form a linearity, especially in the case of small strains.

Structure evolution during deformation was evaluated based on the microstructural observation of metallographic samples at optical microscope Olympus GX-51 and scanning electron microscope JEOL JSM 6460 LV and PHILIPS 535 M with EDAX system for chemical analysis. The samples were etched with 45% CH_3COOH, 35% HNO_3, 10% HCl, and 10% H_3PO_4 to reveal grain boundaries. Observations of fracture surfaces were also performed.

Corrosion-resistance tests of NiAlTiB alloys were conducted in 1-mol solution of H_2SO_4. Polarization curves were obtained by cyclic voltammetry in a classic three-electrode system vented with argon. Venting the solution of sulfuric acid with argon causes the removal of oxygen; thus, the dominating cathodic reaction in an acidic solution is the reduction of hydrogen ions. Taking advantage of voltammetric curves, the following parameters can be established: passivation potential, passivation current and current of solubilizing, which are all responsible for the corrosion resistance of an alloy.

In an electrochemical vessel, a platinum net (antielectrode), working electrode (a sample), and an Ag/AgCl electrode (reference electrode) were placed. The rate of potential change for voltamperometric characeristics was 1V/min.

3. Results and discussion

3.1. Structure and mechanical properties of NiAlTiB alloys

The chemical composition of the studied alloys determined by a scanning electron microscope with EDS is presented in Table 1, while the microstructure micrograph in its initial state are presented in Figure 1.

Table 1. Chemical composition of the studied alloys

Alloy	Content of alloying elements [wt.%]				
	Symbol	Ni	Al	Ti	B
NiAlTiB	A	Bal.	23.0	1.0	0.05
	B	Bal.	22.0	2.0	0.05

Structure observations of the as-cast samples in the sections perpendicular to the direction of pouring melt to a mold are shown in Figure 1. Samples in initial state underwent heat treatment at 1523 K for 48 h, followed by cooling with a furnace to an ambient temperature

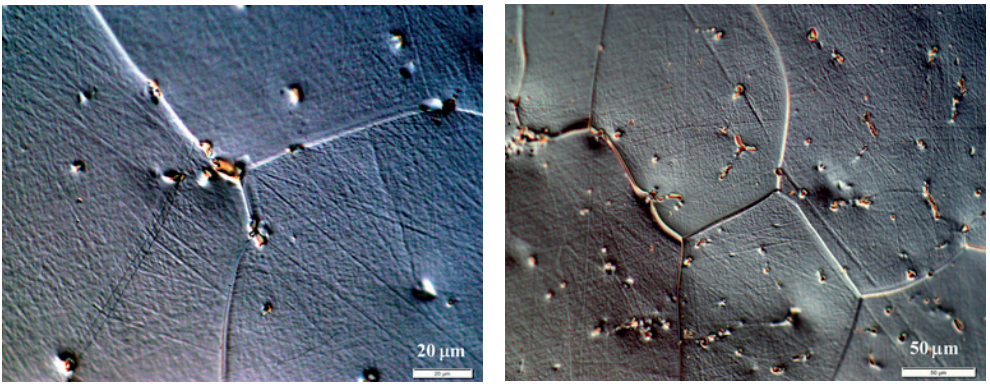

Fig. 1. Microstructures of as-cast samples, sections perpendicular to pouring direction of NiAlTiB alloys: a) A; b) B

X-ray studies allowed us to determine the spacing between planes in crystal lattice d_{hkl} basing on the Bragg's law. Experimental values of interplanar distance and intensities of the studied alloy were compared with values collected in database PDF+4 2006. Recorded diffraction patterns for both alloys prove the formation of an NiAl phase (Fig. 2).

Due to the large amount of experiments conducted, only the chosen cases of compression testing are shown in the paper in the $\sigma = f(\varepsilon)$ oraz $\log\sigma = f(\log\varepsilon)$ coordinate system. Figure 3(a–d) presents true stress-strain characteristics for A and B types of NiAlTiB alloys. Table 2 presents Vickers hardness HV10 and yield strength of alloy B. The determined coefficients of Hollomon equations for each flow curve describing ranges (K_1, K_2, n_1, n_2), and a border between these ranges ($\varepsilon_{1/2,}$ $\sigma_{1/2}$) are collected in the tables, which allows us to present their course in any coordinate system. An example of such a set of Hollomon coefficients is presented in Table 3.

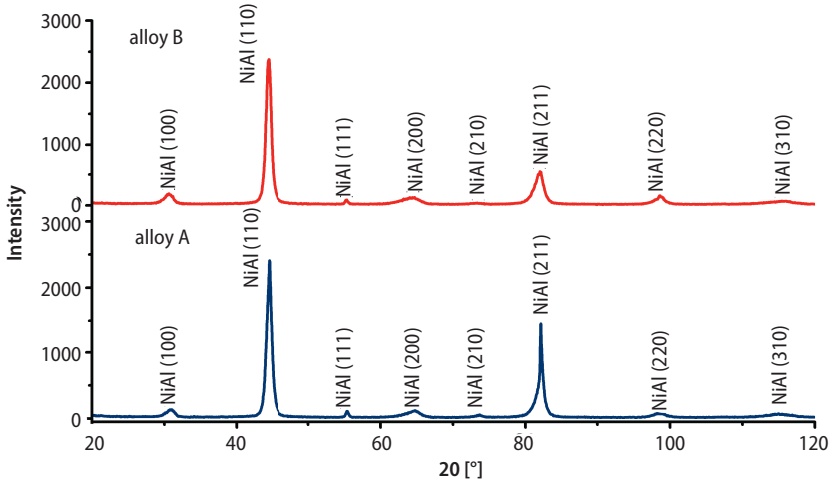

Fig. 2. Diffraction patterns of as-cast NiAlTiB alloys A and B

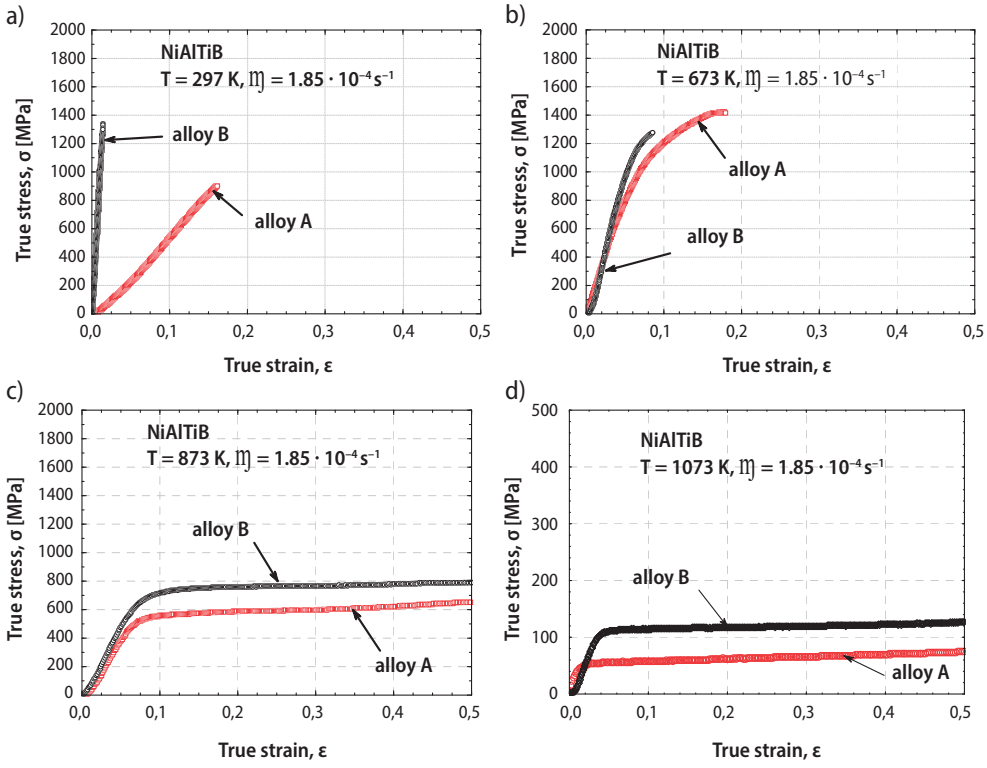

Fig. 3. Deformation characteristics of A and B types of NiAlTiB alloy at temperatures: a) 297 K; b) 673 K; c) 873 K; d) 1073 K; strain rate =1.85·10^{-4} s^{-1}

Table 2. Vickers hardness HV10 and yield points of NiAlTiB – B alloys

Alloy	Hardness HV10	Yield strength R_{02} [MPa]				
		Strain rate $\dot{\varepsilon}$ [s^{-1}]	Temperature T [K]			
			RT	673	873	1073
NiAlTiB (B)	491 ± 8.3 (1.65%)	$9.25 \cdot 10^{-5}$	1064	985	477	102
		$1.85 \cdot 10^{-4}$	1115	1034	592	125
		$1.85 \cdot 10^{-3}$	1140	835	680	142

Table 3. List of coefficients of Hollomon equation

Alloy	$\dot{\varepsilon}$ [s^{-1}] · 1.85	T [K]	K_1 [MPa]	n_1	K_2 [MPa]	n_2	$\varepsilon_{1/2}$	$\sigma_{1/2}$
NiAlTiB (A)	10^{-4}	1073	380.8027	0.4962	67.4373	0.0666	0.0178	51.5600
	10^{-3}	873	5788.9527	0.8034	1369.3044	0.2738	0.0657	649.8455
NiAlTiB (B)	10^{-4}	1073	4959.0670	1.1680	125.8930	0.0426	0.0382	109.5500
	10^{-3}	873	6520.7868	0.8217	1615.4741	0.2872	0.0735	763.2754

The compression tests conducted at room temperature showed small deformation of the A alloy (total elongation $\varepsilon \sim 0.175$). In the case of alloy B, for all initial strain rates ($\dot{\varepsilon}$) almost immediate failure of the samples after achieving certain stress level was observed. The value of maximal stress at which failure occurred is the higher the largest is $\dot{\varepsilon}$. Alloy A was observed to sustain larger strains, while the values of stress are smaller than in the case of alloy B. At higher temperatures, a gradual increase of deformation of both alloys was noted. Besides, the samples did not undergo cracking. The analogous behavior was also observed when the strain rate was changed. Thus, the brittle-ductile transition temperature was defined to be about 673 K and depended on titanium content.

Characteristics presented in a 3-axis coordinate system allowed us to conduct analysis of the dependence of strain in the function of temperature and strain rate. In Figures 4a and b, the dependencies are presented for both alloys in coordination system σ-ε-T and initial strain rate ($\dot{\varepsilon}$) = $1.85 \cdot 10^{-4}$ s^{-1}, which additionally confirms our earlier discussion. On the other hand, Figure 4c presents dependence σ-ε-$\dot{\varepsilon}$ at a constant temperature of 873 K for alloy A in the coordinate system σ-ε-$\dot{\varepsilon}$. No anomalies as those in the alloys with Ni_3Al matrix have been detected. It is also noted that, for higher initial strain rates, higher stresses are recorded (which is additionally confirmed by yield points collected in Table 2). Besides, the results of Vickers hardness HV10 (load 98.07 N) are also listed Table 2). An increase of yield point (at analogous deformation conditions) and

hardness HV10 by almost 7% is observed for alloys with higher titanium content (B alloy). The results for the A alloy were discussed in detail in [16]. The yield point decreases gradually with an increase of temperature until a significant drop is observed at 1073 K (Fig. 4, Tab. 2).

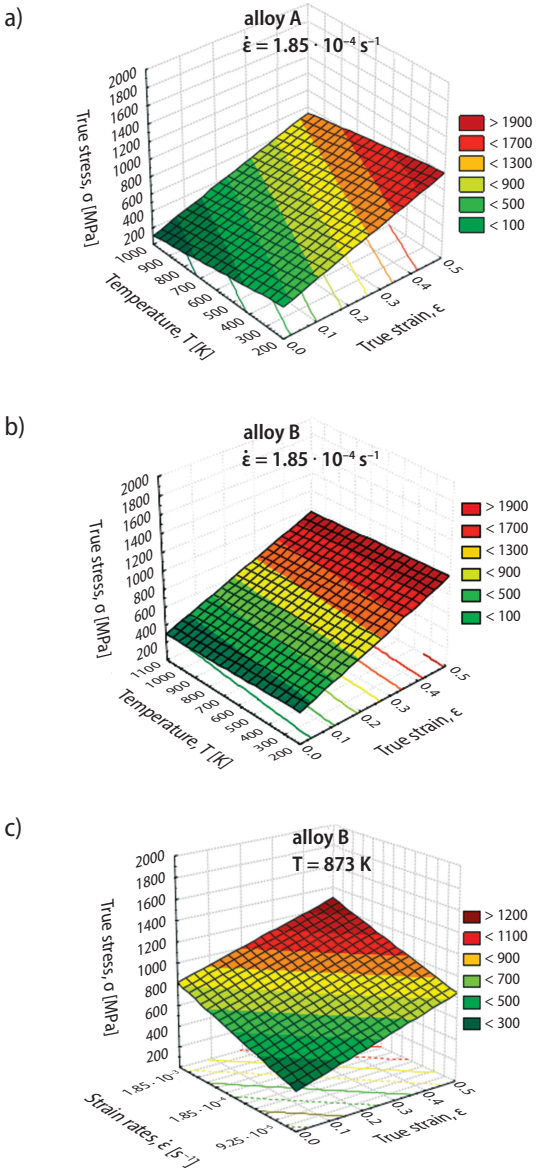

Fig. 4. Deformation characteristics of NiAlTiB alloys in a function of: a) σ-ε-T alloy A, $\dot{\varepsilon} = 1.85 \cdot 10^{-4}\ s^{-1}$; b) σ-ε-T alloy B, $\dot{\varepsilon} = 1.85 \cdot 10^{-4}\ s^{-1}$; c) σ-ε-$\dot{\varepsilon}$ alloy B, T = 873 K

In Figure 5, chosen logσ = f (logε) characteristics of alloys A and B are presented, while in Table 3, Hollomon coefficients describing various ranges (K_1, K_2, n_1, n_2) and border between ranges ($\varepsilon_{1/2}$, $\sigma_{1/2}$) are compiled.

Differences in strength coefficients (K) and hardening exponents (n) for a certain range of hardening depending on test temperature in NiAlTiB alloys (both A and B) were noted. Moreover, higher values of strength coefficients and hardening exponents at a given temperature for the first range of hardening in relation to their equivalents in the second range were observed. Additionally, in most cases, K_2 and n_2 decreased as temperatures increase.

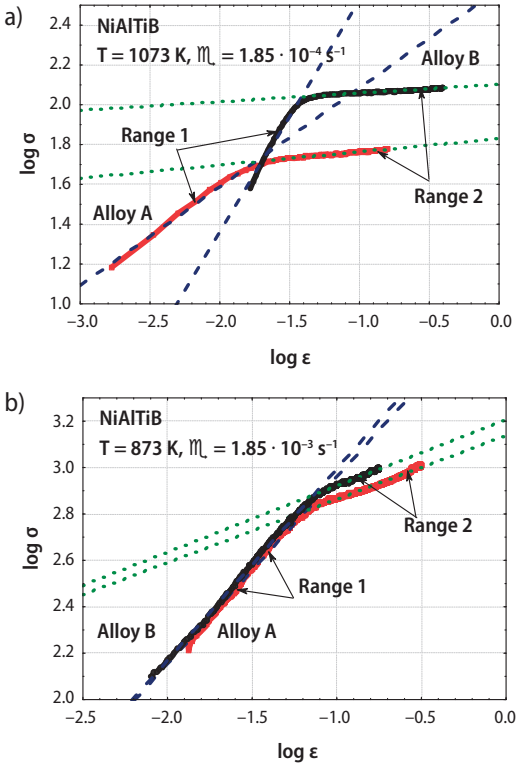

Fig. 5. Characteristics of dependencies log σ = f (logε) for both NiAlTiB alloys

Applying point, linear (Fig. 6) and surface (Fig. 7) analyses by means of the EDS method, it was possible to locate various phases (including that of NiAl). The precipitates present at the grain boundaries as well as inside grains of both types of alloys were identified to be enriched in titanium and boron. Distribution of these regions is inhomogeneous, which is reflected in mappings (Figs 6 and 7). Based on the performed analyses and structure observations, it should be also stated that prolonged annealing at 1523 K is insufficient for the complete homogenization of the alloys.

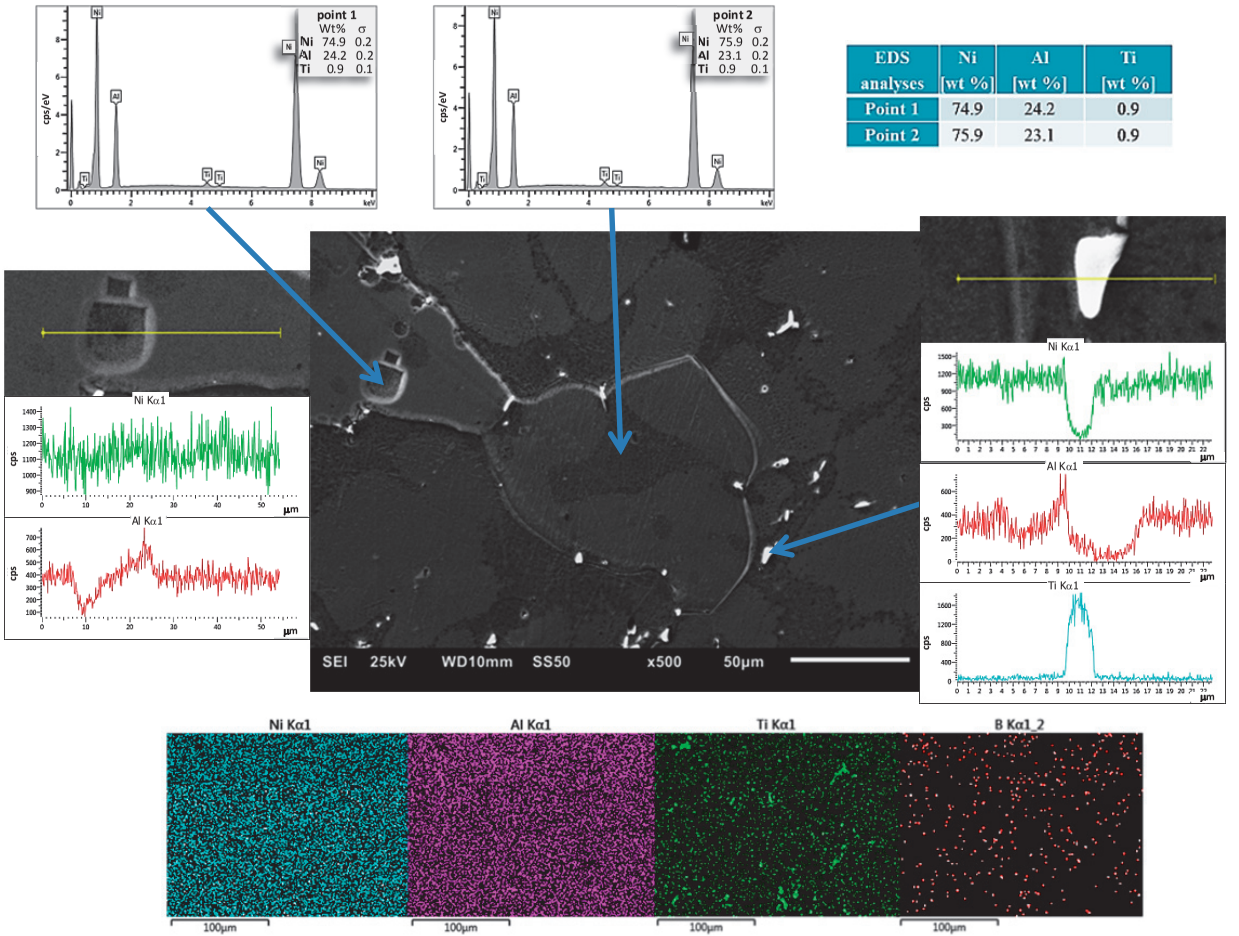

EDS analyses	Ni [wt %]	Al [wt %]	Ti [wt %]
Point 1	74.9	24.2	0.9
Point 2	75.9	23.1	0.9

Fig. 6. Microstructural observations of type A alloy by scanning electron microscope with included EDS analysis

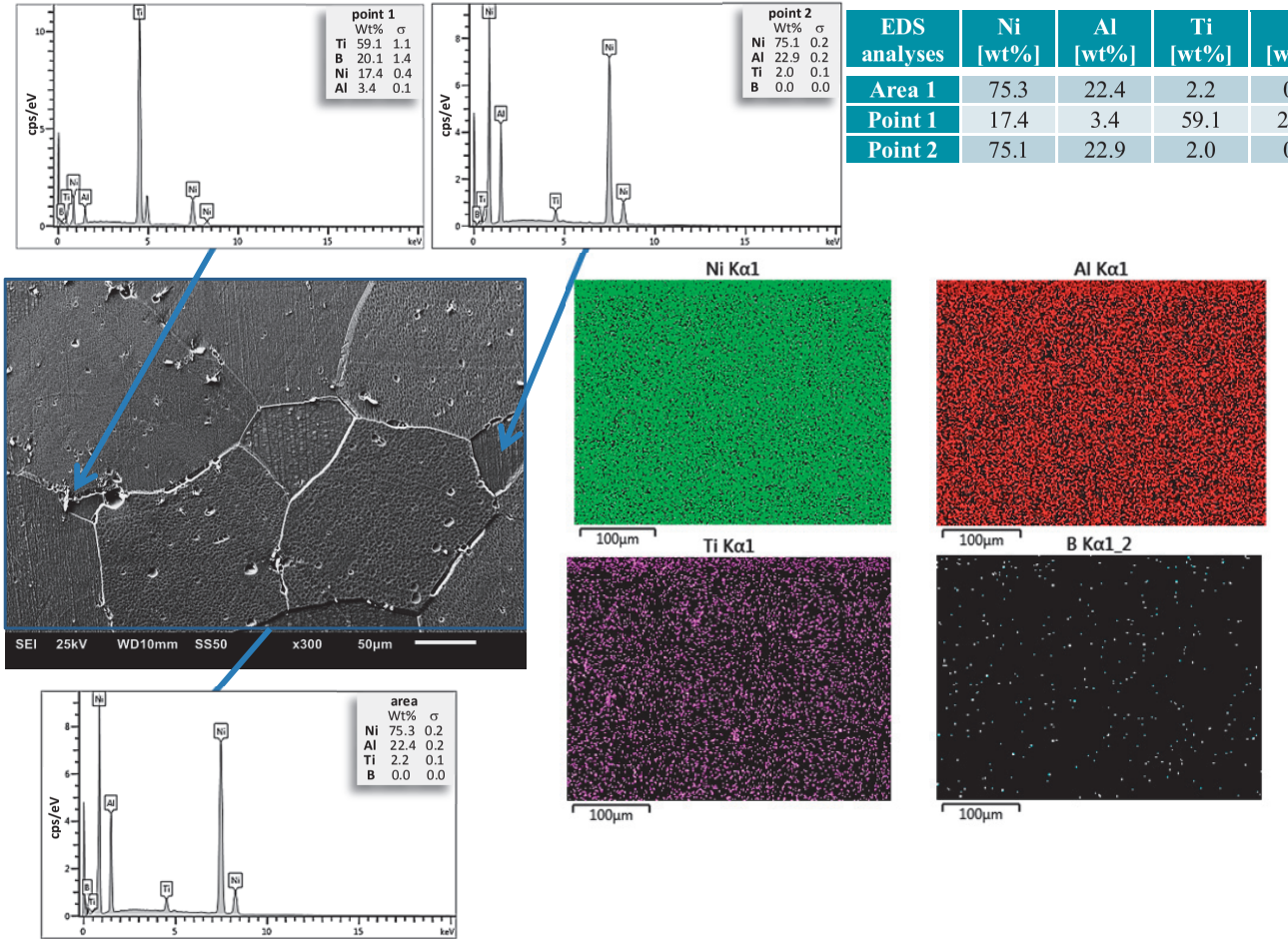

EDS analyses	Ni [wt%]	Al [wt%]	Ti [wt%]	B [wt%]
Area 1	75.3	22.4	2.2	0.0
Point 1	17.4	3.4	59.1	20.1
Point 2	75.1	22.9	2.0	0.0

Fig. 7. Microstructural observations of type B alloy by scanning electron microscope with included EDS analysis

As a result of the performed observations at different levels of deformation, it was found that cracking usually begins at grain boundaries in the case of alloy A (Fig. 8a) and later in regions enriched only by titanium or both titanium and boron (Fig. 8b). Further deformation lead to the inevitable failure of a sample. The before-failure microstructures of alloy A deformed at room temperature ($\varepsilon = 0.15$) and at 673 K ($\varepsilon = 0.17$) are shown in Figures 8b and 8c, respectively.

In the case of alloy B deformed at room temperature, a transcrystalline mechanism of cracking (Figs 9 and 10) was observed.

Similarly, the before-failure microstructures of alloy B deformed at 673 K ($\varepsilon = 0.07$) is shown in Figure 11.

Fractures characteristic of brittle failure of the samples deformed at temperatures of 297 K and 673 K for alloy A and B, respectively, are presented in Figure 12. Samples made of alloy B and deformed at room temperature encountered complete damage. On the other hand, samples of both alloys deformed at temperatures of 873 K and 1073 K, respectively, deformed without failure.

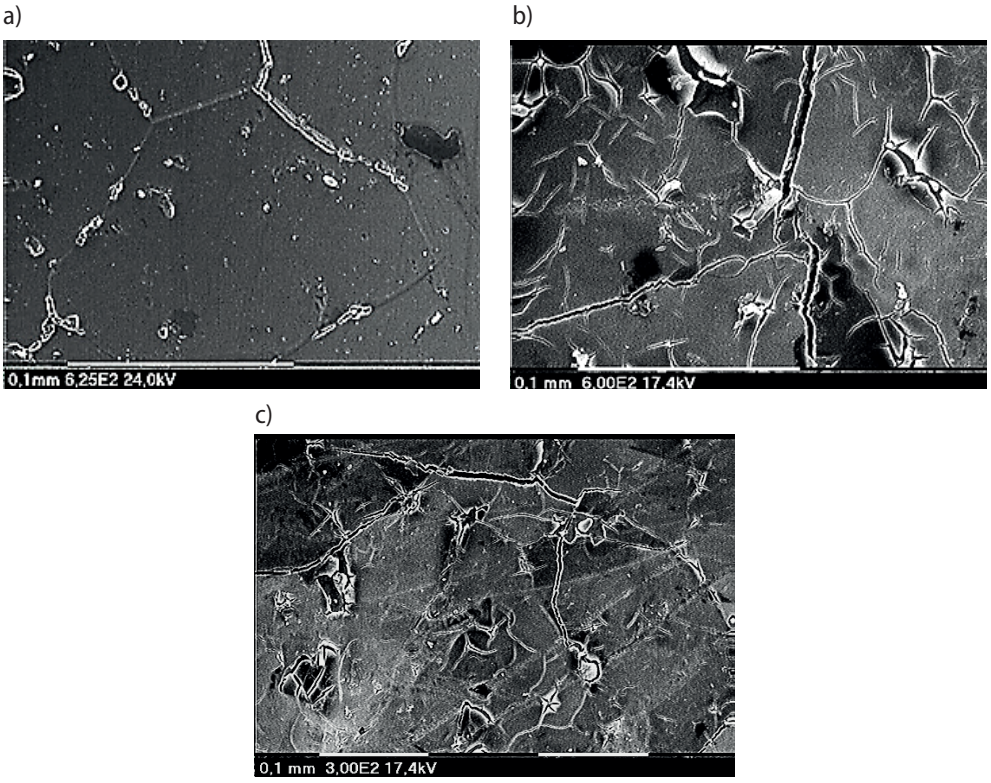

Fig. 8. Microstructural observations of type A of NiAlTiB alloy by scanning electron microscope: a) room temperature, $\varepsilon = 0.005$; b) room temperature, $\varepsilon = 0.15$; c) temperature of 673 K, $\varepsilon = 0.17$

a) b)

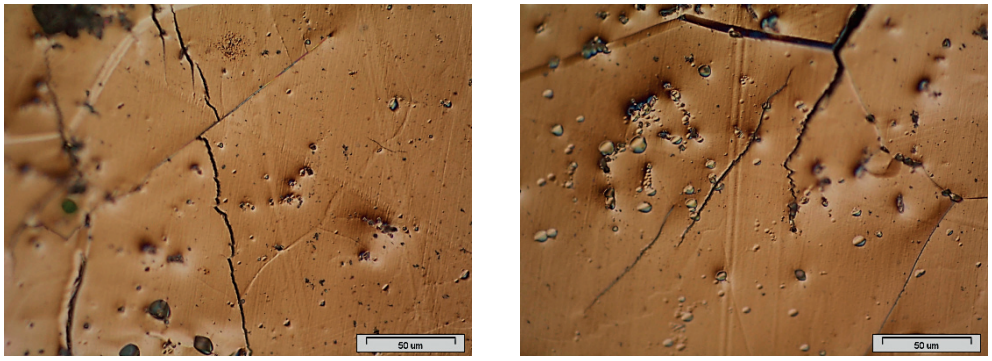

Fig. 9. Microstructural observations of type B of NiAlTiB alloy by optical microscope, room temperature, ε = 0.005

a) b)

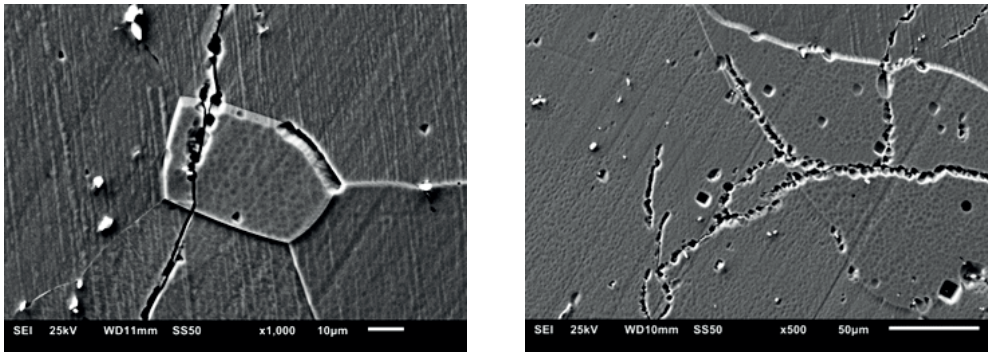

Fig. 10. Microstructural observations of type B of NiAlTiB alloy by scanning electron microscope, room temperature, ε = 0.005

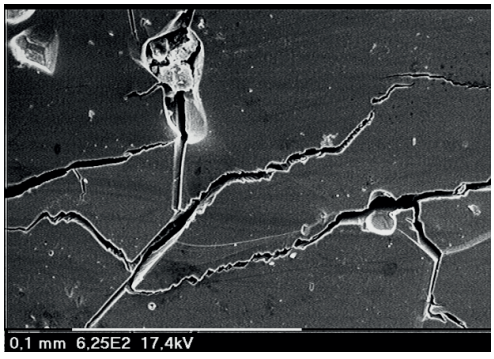

Fig. 11. Microstructural observations of type B of NiAlTiB alloy by scanning electron microscope, temperature of 673 K, ε = 0.07

a)

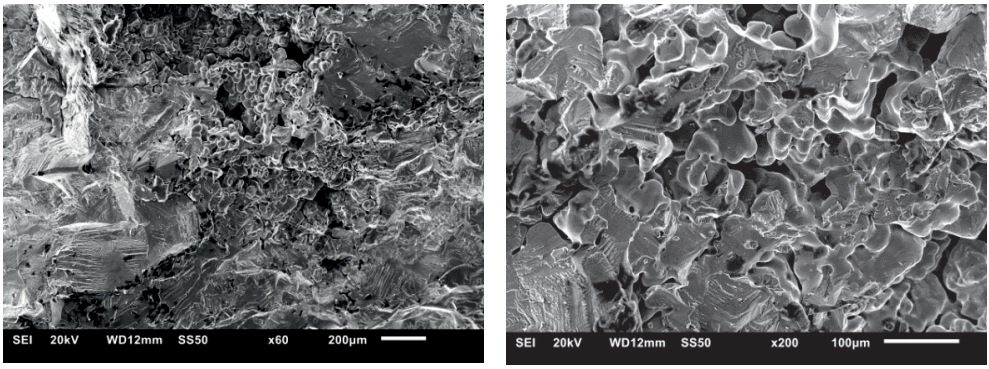

b)

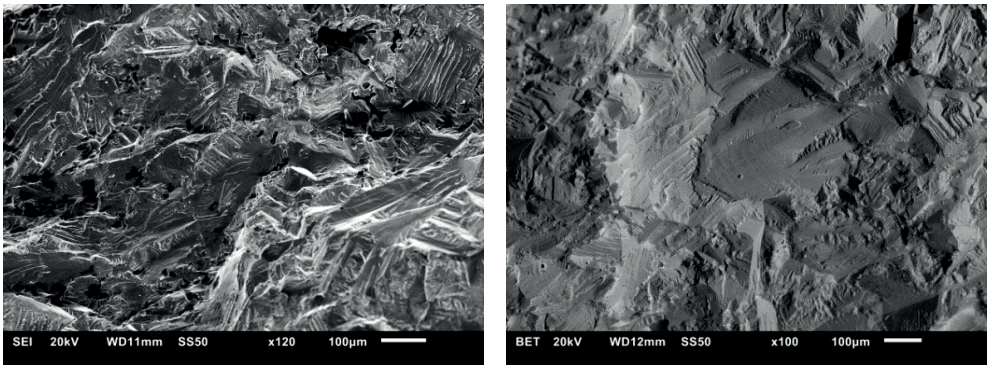

Fig. 12. Fracture micrographs of NiAlTiB alloys: a) alloy A deformed at 297 K; b) alloy B deformed at 673 K

3.2. Resistance to corrosion in NiAlTiB alloys

In Figure 13, corrosion potentials of NiAlTiB alloys appear to reach a constant value after 500 s. Values of the corrosion potentials of the samples are equal to -0.262 and 0.254 V for alloy A and B, respectively. In order to determine corrosion resistance of the alloys, voltammetric curves were prepared in a 1-mol solution of sulfuric acid, which are presented in Figure 14. The polarization curves of alloys containing titanium exhibit the presence of a small peak of active solubilizing at potential about 0V with respect to the Ag/AgCl electrode. Maximal current of the peak for both alloys is 2 mA/cm^2; then, it decreases and keeps a constant value at a wide range of potentials. The peak of active solubilizing is connected with the formation of a layer of corrosion products made from a mixture of nickel and aluminium oxides, which block the surface of the alloy. The presence of titanium significantly prohibits anodic solubilization of the alloy (small peak at polarization curve). The value of the corrosion potential of both alloys proves that the alloy is not subjected to active solubilization. E_{kor} reaches a value of potential in the region before active solubilization.

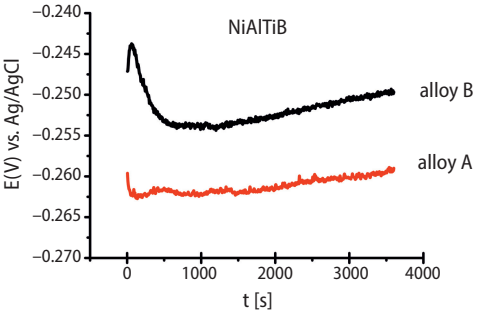

Fig. 13. Corrosion potential of NiAlTiB alloys measured in 1M H_2SO_4 solution

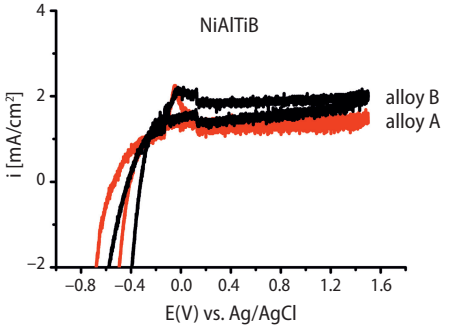

Fig. 14. Voltammetric curves for NiAlTiB alloy A and B with potential rate of 1V/min in 1M H_2SO_4 solution

A characteristic feature is the lack of peaks of cathodic reduction at the backward curve. Such behavior suggests that anodic solubilization of the alloy and the formation of corrosion products is an irreversible process.

4. Conclusions

It is possible to produce alloys on the basis of the NiAl matrix by means of the Exomelt cost-saving process. The obtained alloys are characterized by compact structure with homogeneously distributed regions enriched in titanium. Due to the application of this method, it becomes possible to shorten the production time of the alloy; thus, saving about 40% of energy.

The addition of titanium and boron causes embrittlement at room temperature; however, it influenced the improvement of mechanical properties at higher temperatures. At a temperature of 673 K or higher, it has been shown to increase plasticity, and the addition of titanium and boron resulted in an increase of strength. At temperatures of 873 and 1073 K, there was no destruction of samples in the compression test. Alloying additions resulted in an increase in hardness.

The conducted electrochemical studies of corrosion resistance of NiAlTiB alloys show that they undergo active solubilizing followed by the formation of a layer of corrosion products. The mentioned process is irreversible due to the lack of cathodic reduction peaks on the backward curve. The alloying addition remarkably influences corrosion resistance of Ni-Al alloys; e.g., alloys containing Ti are resistant to corrosion in sulfuric acid. Titanium oxide forming at the surface protects the alloy from active solubilizing.

Acknowledgements

This work was carried out with financial support through statutory funds of Pedagogical University in Krakow.

References

[1] Darolia R.: NiAl Alloys for high-temperature structural applications. JOM 43, 3 (1991), 44–49
[2] Trinh D., Műller M.: Aluminides, 4H1609 Functional Materials, Project report, KTH 2002
[3] Frommeyer G., Rablbauer R.: High Temperature Materials Based on the Intermetallic Compound NiAl Reinforced by Refractory Metals for Advanced Energy Conversion Technologies, Materials Technology. Steel Research International, 79, 7 (2008), 507–513
[4] Bojar Z., Przetakiewicz W. (red.): Materiały metalowe z udziałem faz międzymetalicznych. Wydawnictwo BEL Studio, Warszawa, 2006
[5] Noebe R.D., Bowman R.R., Nathal M.V.: The Physical and Mechanical Metallurgy of NiAl. Physical Metallurgy and Processing of Intermetallic Compounds, 1996, 212–296
[6] Hawk J.A., Alman D.E.: Abrasive wear behaviour of NiAl and NiAl-TiB_2 composites. Wear, 225–229 (1999), 544–556
[7] Colin J., Serna S., Campillo B., Flores O., Juárez-Islas J.: Microstructural and lattice parameter study of as-cast and rapidly solidified NiAl intermetallic alloys with Cu additions. Intermetallics, 16, 7 (2008), 847–853
[8] Zhou J., Guo J.T.: Effect of Ag alloying on microstructure, mechanical and electrical properties of NiAl intermetallic compound. Materials Science and Engineering A, 339 (2003), 166–174
[9] Hyjek P., Sulima I., Figiel P.: NiAl composite reinforced TiB_2 ceramic particles. In: M. Szutkowska (ed.), Innovative Manufacturing Technology 2013, The Institute of Advanced Manufacturing Technology, Krakow 2013, 31–42
[10] Shi-xiang Hou, Zong-de Liu, Dong-yu Liu: The study of NiAl-TiB2 coatings prepared by electro-thermal explosion ultrahigh speed spraying technology. Surface & Coatings Technology, 205 (2011), 4562–4568
[11] Hyjek P., Kurtyka P., Wierzbiński S., Krawiec H.: Odporność korozyjna kompozytów na osnowie stopu Al-Zn-Mg wzmacnianych cząstkami Al_2O_3, Kompozyty, 5, 2 (2005), 43–46
[12] Białobrzeski A., Czekaj E., Heller M.: Corrosive behaviour of aluminium and magnesium alloys processed by die casting technology. Archives of Foundry, 2, 3 (2002), 294–313
[13] Kmita A., Janas A., Hutera B.: Synthesis and evaluation of the structure of Ni_3Al/C alloy. Metallurgy and Foundry Engineering, 35, 2 (2009), 147–154
[14] Krupkowski A.: The deformation of plastic metals by strain. Annales de l'Académie Polonaise des Sciences Techniques, 7 (1946), 113–118
[15] Ludwigson D.C.: Modified stress-strain relation for FCC metals and alloys. Metallurgical Transactions, 2 (1971), 2825–2828
[16] Hyjek P., Sulima I.: Microstructure and mechanical properties of Ni-Al-Ti-B alloy. Ores and Non-Ferrous Metals, 60, 5(2015), 211–217

Metallurgy and Foundry Engineering – Vol. 41, 2015, No. 1, pp. 45–56
http://dx.doi.org/10.7494/mafe.2015.41.1.45

Aldona Garbacz-Klempka, Stanisław Rzadkosz, Tomasz Stolarczyk, Janusz Kozana, Marcin Piękoś, Zofia Kwak, Mieszko Tenerowicz

Computer modeling for the visualization and geometric reconstruction of artefacts from the casting workshop in Grzybiany

Modelowanie komputerowe do wizualizacji oraz rekonstrukcja geometryczna zabytków z pracowni odlewniczej Grzybiany

Abstract

The casting workshop in Grzybiany is one of the most important archaeological sites in regards to casting technology from the Bronze and Early Iron Ages. During the "Grzybiany. Osada nadjeziorna z epoki brązu i żelaza" [Grzybiany. Lakeside settlement from the Bronze and Early Iron Ages] research, the structure of casting moulds was analyzed as well as the chemical composition and microstructure of one of the more-interesting metal artefacts found within the workshop. Based on this, geometric visualization was performed with the help of computer-modeling methods. For scientific, experimental, and educational purposes, reconstruction of a zoomorphic pendant was performed using the lost-wax method. Wax models injected into a matrix were used, along with fired ceramic (gypsum) moulds and a specially prepared modeling alloy that corresponds to the original material. In this way, a true replica of the original was obtained: technologically, structurally and chemically.

Studies of production technology of the casting workshop dated back to the Bronze and Early Iron Age help to increase the knowledge of the mould-preparing technology and the alloys used. Modern tools and computer programs aid in the research of old technologies and help disseminate the results.

Keywords: archaeometallurgy, casting, lost-wax method, bronze, computer modelling, 3D visualization

Aldona Garbacz-Klempka Ph.D. Eng., Stanisław Rzadkosz Prof. Ph.D, D.Sc. Eng., Janusz Kozana Ph.D. Eng., Marcin Piękoś M.Sc. Eng., Zofia Kwak M.Sc. Eng.: AGH University of Science and Technology, Faculty of Foundry Engineering, Historical Layers Research Centre, Krakow, Poland; agarbacz@agh.edu.pl; **Mieszko Tenerowicz M.Sc. Eng.:** AGH University of Science and Technology, Faculty of Foundry Engineering, Krakow, Poland; **Tomasz Stolarczyk Ph.D.:** Copper Museum in Legnica, Legnica, Poland; archeologia@muzeum-miedzi.art.pl

Streszczenie
Pracownia odlewnicza w Grzybianach należy do jednego z najważniejszych stanowisk archeologicznych pod względem studiów nad technologią odlewniczą w epoce brązu i wczesnej epoce żelaza. W toku prac wykonano analizę struktury form odlewniczych. Przeprowadzono także analizę składu chemicznego i mikrostruktury jednego z ciekawszych zabytków metalowych, odkrytych na terenie pracowni. Na tej podstawie, z wykorzystaniem metod modelowania komputerowego, wykonano wizualizację geometryczną. W celach naukowych, doświadczalnych i edukacyjnych wykonano rekonstrukcję zawieszki zoomorficznej przy wykorzystaniu metody wytapianych modeli. Zastosowano modele woskowe wtryskiwane do matrycy, formy ceramiczne (gipsowe) wypalane oraz specjalnie przygotowany stop modelowy, odpowiadający oryginalnemu. W ten sposób uzyskano wierną technologicznie, strukturalnie i chemicznie replikę zabytku.

Badania technologii produkcji warsztatu odlewniczego z epoki brązu i wczesnej epoki żelaza przyczyniają się do wzrostu świadomości o stosowanych technikach przygotowania form i wykorzystywanych stopach. Współczesne narzędzia i techniki komputerowe wspomagają badania dawnych technologii i służą ich upowszechnianiu.

Słowa kluczowe: archeometalurgia, odlewnictwo, metoda wytapianych modeli, brąz, modelowanie komputerowe, wizualizacje 3D

1. Introduction

Archaeological research in the area of a late Bronze – early Iron Age settlement in Grzybiany (in the Legnica district of Poland) belongs to the most important discoveries in Lower Silesia [1–5]. It is an important element of research of the development of casting techniques, because of the number and technological character of the artefacts. The settlement area, located on the headland extending into Koskowickie Lake, was first excavated during the years 1959–1962 [5]. The research was renewed by the *Institute of History of Material* Culture of the Polish Academy of Sciences in Warsaw, and was conducted over the next seven seasons (1970–1973, 1977–1980) under the direction of Zbigniew Bukowski [3].

Clay casting moulds, the first objects testifying to the manufacturing character of the settlement, were discovered in its central part. Next, a significant concentration of casting workshop remnants that operated here were recognized: castings ladles, tuyeres, metal artefact fragments, casting moulds, and formations testifying to conducting fire processes (roasted clay, hearth remnants). Based on the analysis of mobile artefacts and special analysis, the collection of finds from the workshop area, has been dated to the 6^{th}–5^{th} century BC [1].

Since 2013, these artefacts have been researched by the Copper Museum in Legnica, the Archaeology Institute of Wroclaw University and the Faculty of Foundry Engineering of AGH - University of Science and Technology in Krakow.

The collection of artefacts from Grzybiany was analyzed in detail due to their connection with casting technology. The artefacts researched are considered to belong to a mould preparation and lost-wax casting workshop [6–10]. The moulds from Grzybiany

are disposable, as they were made from a mixture of sand (with differing grain sizes) and clay (Figs 1–4). A mould was prepared by covering a wax model with clay or stamping previously prepared and fired clay models in moist clay.

Fig. 1. Part of casting mould (accession no. 44/77)

Fig. 2. Part of casting mould (accession no. 87/77)

Fig. 3. Macroscopic picture of mould (accession no. 64/78) different sizes of sand grains visible, magnification 7×

Fig. 4. Macroscopic picture of mould (accession no 64/78) different sizes of sand grains visible, magnification 50×

In the workshop area, metal objects and their fragments were also discovered, and their condition suggests that they were damaged as early as in their production stages. By applying proper computer tools, they can be reconstructed so to be conducive to a more-complete analysis of the process. Archaeometallurgical research contributes to learning about and reconstructing the elements of the old technology [11]. A great role in the reconstruction of artefacts is played by computer programs, which help to transfer historical artefacts into a virtual environment [12].

Helpful for research as well as the dissemination of results, 3D visualizations made on the bases of detailed photographs are used for documenting purposes. To analyze the artefacts that are to be cast from a technological perspective, design drawings have to be prepared, using the appropriate tools. Here, the Blender program was used (Blender is a freeware program for creating three-dimensional graphics). Due to its atypical interface, the program may pose some difficulties; however, it is universal and offers a broad scope of possibilities (like 3D modelling, rendering, and animation making). When recreating the technology for making a specific artefact, the cast itself was not only modeled, but also its mould, core and gating system. This allowed us to create an assembly drawing. A 3D reconstruction prepared in this way and saved in the appropriate format enables us to transfer the process of pouring liquid metal into a mould to the simulation environment (using MAGMASOFT, Flow-3D or Pro-CAST) or to tools that enable 3D printing.

2. Methodology

A set of casting moulds and metal artefacts from archaeological research at the Grzybiany settlement was researched. Their technology was assessed based on the analysis of the surface, structure and microstructure of the casts. There were macro- and microscopic

analyses using light microscopy. Also, qualitative and quantitative tests of chemical composition were conducted with the help of the XRF method. Based on the macrostructure analyses of the artefacts, their 3D visualizations, designs, and 3D prints were prepared. The goal was to recreate the casting technology of the ornamental objects with the help of modern engineering programs. An important task was to reconstruct a zoomorphic pendant using the lost-wax casting method.

3. Researching the chemical composition and structure

In the workshop area, numerous objects (mainly ornaments) were found. The shapes of some of them match the mould fragments, which proves that not only the moulds were prepared in this workshop in Grzybiany, but also the casts. The research showed that the casts were made from copper alloys with varying chemical compositions. There were two-component alloys present of Cu-Sn type, three-component Cu-Sn-Pb, but also multi-component ones, where the presence of Sb, As, Fe and others should be seen as a technological reminder of obtaining raw materials from polymetallic ores. An example of this chemical composition was a small zoomorphic casting (Fig. 5).

Fig. 5. Macroscopic photo of zoomorphic pendant (accession no. 300/78)

The zoomorphic pendant was made using the lost-wax method, as a precision casting in clay mould. Chemical composition tests showed (Fig. 6) that the pendant was made from tin bronze of Cu-Sn type, with the addition of lead as well as a significant share of iron, antimony, nickel and arsenic.

Microscopic pictures (Figs 7 and 8) of surface fragments of the zoomorphic cast show structural elements of regular shapes and relatively high compactness and homogeneity. The fine-grained structure has a dendritic character. Light phases of the components are located in the dendritic spaces, against which there are primary dendritic crystallites of dark hue visible, spaced in an uneven manner.

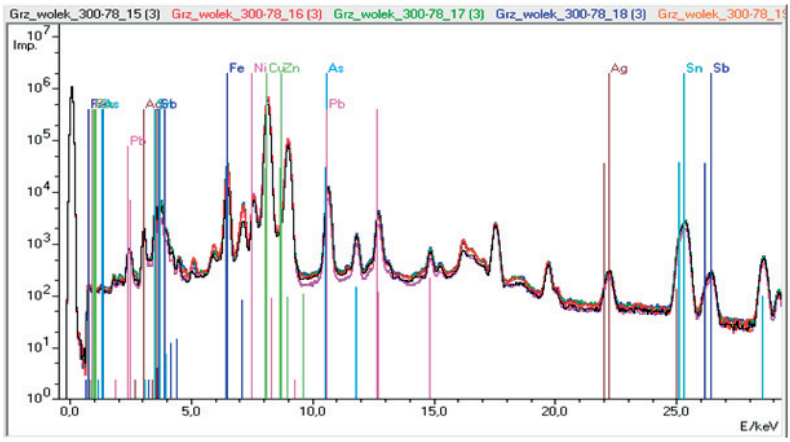

Fig. 6. Fluorescent spectrum of the zoomorphic pendant: C, Sn, Pb, Sb, As, Ni, Fe, Ag and Zn were identified

a) b)

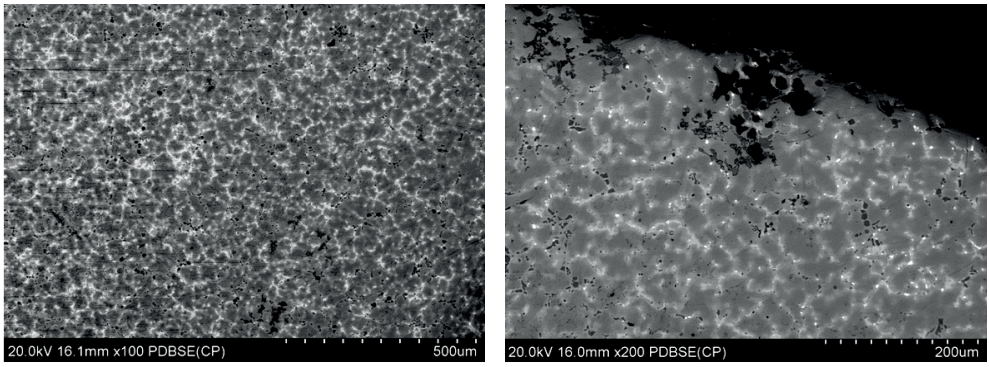

Fig. 7. SEM micrograph: a) center of the sample, magnification 100×; b) at the edge of the sample, magnification 200×

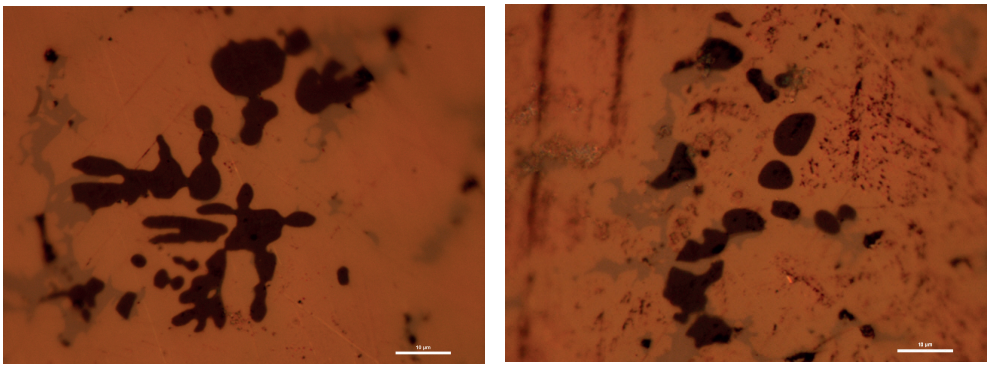

Fig. 8. Zoomorphic pendant microstructure, different shape of precipitates

4. Visualization based on computer modelling

To visualize and recreate the production technology of the casts researched, computer modeling methods were applied. The visualization of artefacts was made for documentation, research, and disseminating purposes. Prior to starting the project, it was necessary to make reference pictures (Fig. 9) that enabled observation of the model during the design process. This made it possible to transfer the artefact into virtual space. This was one of the stages leading to the implementation of model reconstruction of the artefact using modern computer software.

Then, in graphics program Blender 2.69, a symmetrical block was formed that corresponded approximately to the pendant shape (Fig. 10a). The method used for creating this is called box-modeling, and a more-streamlined shape was obtained using a Multiresolution modifier. Thus prepared, the model could be further converted by a virtual-sculpting method. This has resulted in a more-accurate shape as well as showing more-prominent irregularities of the surface. After that, the model was no longer symmetrical (Fig. 10b). The final stage was its grid preparation for applying the texture. It was applied with an additional script called BProjection. After applying the texture and bump mapping, the model was ready to perform the rendering (Fig. 10c).

Fig. 9. Exemplary reference picture

Fig. 10. Computer modelling of the pentant: a) symmetrical model of the pendant roughly corresponding to the original; b) finished model sharped by sculpting, without textures; c) finished model, after adding the texture and bump mapping

Fig. 11. Computer visualization of zoomorphic pendant reconstruction

For taking pictures, it was necessary to create a proper scene. The cycles rendering engine was used. The visualization is presented below (Fig. 11).

At the same time, the models were prepared (Fig. 12), which were then transferred to the software cooperating with a 3D printer. The ABS (*Acrylonitrile Butadiene Styrene*) prints recreated the geometry of the object (Fig. 13).

Fig. 12. Visualization prepared for 3D printing

Fig. 13. 3D printing with ABS

5. Geometric reconstruction of the pendant using the lost-wax method

One of the most important objectives of the research was making a pendant copy at the same scale from recreated material and (what was paramount) utilizing the lost-wax casting method. For this end, computer 3D visualizations were used, which enabled us to make 3D model prints from ABS material.

At the same time, a matrix was made from the natural model with Castaldo Rapid rubber (hardenable by vulcanization), ensuring high fidelity of the recreated detail. The matrix recreated the shape and texture of the zoomorphic pendant (Fig. 14a). Ruby Red modeling wax, characterized by minimal shrinkage and precise detail rendering, was injected into the matrix.

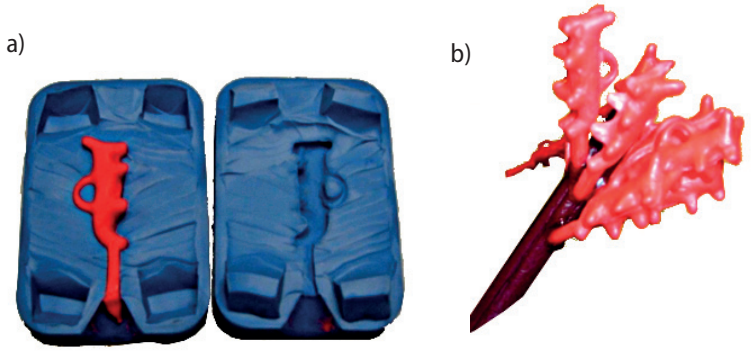

Fig. 14. Matrix for making the wax models (a), modelsconnected with the gating system (b)

Fig. 15. Unpolished cast (a), finished casts (b)

The finishing work consisted only of cutting the gating system off and cleaning and polishing the cast surface. In this way, the cast geometry, its texture and also small casting flaws were copied from the original (Fig. 15).

Wax models that were prepared in this way were joined into a pattern set (Fig. 14b), which was used for making the casting mould. Satin Cast gypsum mass was used for this purpose, the material commonly accepted as yielding the best results and ideal casts.

Once prepared, the mould was subjected to drying and heating according to the set parameters of temperature increase in time (Fig. 16a). The mould was filled (Fig. 16b) with the modeling alloy that had a temperature of 1140°C. This alloy, created according to the formula resulting from research of the chemical composition of the zoomorphic pendant, was determined as multicomponent bronze, consisting of copper, tin, antimony, arsenic, nickel, silver and iron.

a) b)

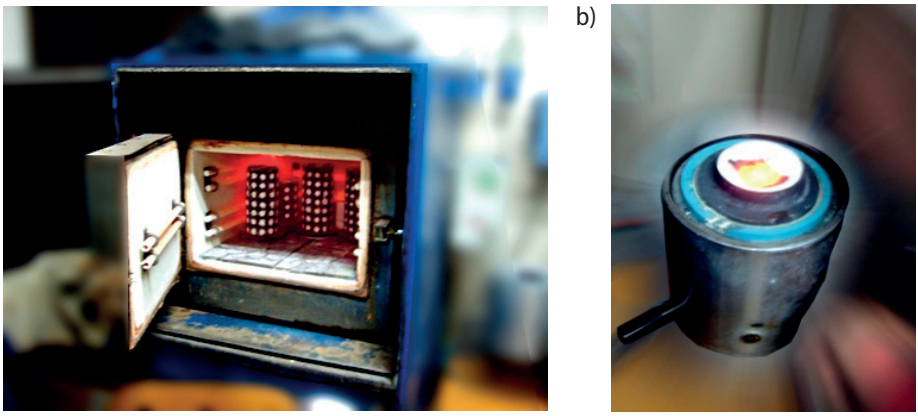

Fig. 16. Firing the moulds (a), Pouring the modelling alloy – multicomponent bronze (b)

The necessity of using high-quality materials resulted from the need to ensure the maximum likeness between the copy and the original pendant.

6. Conclusions

The casting workshop in Grzybiany near Legnica belongs to one of the most significant archaeological sites from the perspective of studies on casting technology in the Bronze and early Iron Ages. During the research of the artefacts from Grzybiany, various analytical and visualization methods were applied. The main goal of the research was analyzing the casting technology used in the workshop under scrutiny, allowing recreating one of the important metal artefacts. A series of tests on casting moulds was conducted, which proved that the lost-wax casting method was used in the Grzybiany workshop. The research of metal artefacts allowed us to assess the alloys used there. For scientific, experimental, and educational purposes a computer visualization was performed, and the zoomorphic pendant was next reconstructed using the lost-wax method.

The article points to the fact that computer programs play an important role in artefact reconstruction, thus enabling the transfer of historical elements into the CAD

environment which, in turn, results in the possibility of further modifications. Once prepared, three-dimensional reconstruction recorded in the appropriate format enables its transfer into the simulation environment of casting liquid metal into the mould (using the MAGMASOFT, FLOW-3D or ProCAST programs) or using tools for 3D printing. Because of their specific shapes, historical artefacts are often impossible to recreate with the use of typical industrial programs. Due to the way the model is created as well as its full grid control, artistic programs such as Blender offer the possibility of reproducing such complicated shapes as the one presented in the article.

Wax models injected into the mould were used, ceramic (gypsum) fired moulds and modelling alloy, prepared according to the formula based on the analysis of chemical composition of the pendant. In this way, a technologically-, structurally-, and chemically-true replica of the pendant was obtained, as well as its computer visualization.

The lost-wax casting method is used in metal artefacts reconstruction because of good dimensional and surface repeatability. The obtained casts keep analogies to the original as far as the texture and small casting faults are concerned, testifying to the old technologies.

References

[1] Stolarczyk T., Baron J. (red.): Osada kultury pól popielnicowych w Grzybianach koło Legnicy. Muzeum Miedzi w Legnicy, Legnica – Wrocław, 2014

[2] Gedl M.: Zarys dziejów metalurgii miedzi i brązu na ziemiach polskich do początku epoki żelaza. Pamiętnik Muzeum Miedzi, tom I. Legnica, Wydawnictwo Towarzystwa Przyjaciół Nauki w Legnicy, 1982, 33–65

[3] Bukowski Z.: Osiedle otwarte kultury łużyckiej w Grzybianach, woj. legnickie w świetle dotychczasowych badań. Pamiętnik Muzeum Miedzi, tom I. Legnica, Wydawnictwo Towarzystwa Przyjaciół Nauki w Legnicy, 1982, 13–29

[4] Gajewski L.: Ślady obróbki miedzi i jej stopów z wczesnej epoki żelaza w Grzybianach koło Legnicy. Pamiętnik Muzeum Miedzi, tom I. Wydawnictwo Towarzystwa Przyjaciół Nauki w Legnicy, 1982, 147–155

[5] Hensel Z.: Technologie odlewnictwa brązu na podstawie znalezisk w Grzybianach koło Legnicy. Pamiętnik Muzeum Miedzi, tom I. Legnica, Wydawnictwo Towarzystwa Przyjaciół Nauki w Legnicy, 1982, 157–166

[6] Baron J., Stolarczyk T.: Wznowienie badań wykopaliskowych na osadzie z epoki brązu i wczesnej epoki żelaza w Grzybianach w powiecie legnickim. Śląskie Sprawozdania Archeologiczne, 54 (2012), 101–127

[7] Rzadkosz S., Zych J., Garbacz-Klempka A., Kranc M., Kozana J., Piękoś M., Kolczyk J., Jamrozowicz Ł., Stolarczyk T.: Copper alloys in investment casting technology. Metalurgija, 54, 1 (2015), 293–296

[8] Garbacz-Klempka A., Rzadkosz S.: Charakterystyka składu chemicznego i struktury zabytków metalowych z osady kultury łużyckiej w Grzybianach. Osada kultury pól popielnicowych w Grzybianach koło Legnicy. Muzeum Miedzi w Legnicy, Legnica – Wrocław, 2014, 507–538

[9] Garbacz-Klempka A., Rzadkosz S.: Analiza technologii odlewania z epoki brązu i wczesnej epoki żelaza na podstawie form odlewniczych w osady kultury łużyckiej w Grzybianach. Osada kultury pól popielnicowych w Grzybianach koło Legnicy. Muzeum Miedzi w Legnicy, Legnica – Wrocław, 2014, 539–565
[10] Rzadkosz S.: Odlewnictwo miedzi i jej stopów. Wydawnictwo Naukowe Akapit, Kraków, 2013
[11] Roberts B.W., Thornton C.P.: Archaeometallurgy in Global Perspective. Methods and Syntheses. Springer, New York, 2014.
[12] Garbacz-Klempka A., Szucki M.: Computer modelling in visualisation and reconstruction of archeological relicts. Archives of Metallurgy and Materials, 54, 2 (2009), 339–345

Metallurgy and Foundry Engineering – Vol. 41, 2015, No. 1, pp. 7–16
http://dx.doi.org/10.7494/mafe.2015.41.1.7

Remigiusz Kowalik, Dawid Kutyła, Krzysztof Mech, Mirosław Wróbel, Tomasz Tokarski, Piotr Żabiński

Electrochemical codeposition of molybdenum and selenium

Elektrochemiczne osadzanie molibdenu z selenem

Abstract
The electrodeposition of Mo-Se thin films from a sulfate solution containing Na_2MoO_4 and H_2SeO_3 was studied. The process of deposition was conducted under potentiostatic conditions on a copper electrode. The effect of potential value, pH, and time of deposition were examined. The deposits were characterized by X-ray diffraction, X-ray fluorescence, and scanning electron microscopy. The obtained results have shown the possibility of co-deposition of molybdenum and selenium with different stoichiometric ratios.

Keywords: electrodeposition, molybdenum, selenium, transition metal chalcogenides

Streszczenie
Przeprowadzono badania dotyczące procesu elektrochemicznego osadzania molibdenu z selenem z roztworów siarczanowych zawierających Na_2Mo_4 i H_2SeO_3. Proces osadzania przeprowadzono w warunkach potencjostatycznych na elektrodach miedzianych. Zbadano wpływ potencjału, pH elektrolitu oraz długości czasu osadzania na jakość otrzymanych powłok. Otrzymane warstwy były badane z wykorzystaniem dyfrakcji rentgenowskiej, spektrofluorymetrii rentgenowskiej oraz skaningowego mikroskopu elektronowego. Wykazano możliwość otrzymania powłok o różnym stosunku molibdenu do selenu.

Słowa kluczowe: elektroosadzanie, molibden, selen, chalkogenki metali przejściowych

1. Introduction

Transition metal chalcogenides are a wide group of compounds that have band gaps from 0 to 2 eV with very promising optoelectronic properties, enabling the transition

Remigiusz Kowalik Ph.D. Eng., Dawid Kutyła Eng., Tomasz Tokarski Ph.D. Eng., Piotr Żabiński Ph.D. D.Sc.: AGH University of Science and Technology, Faculty of Non-Ferrous Metals, Krakow, Poland; **Krzysztof Mech Ph.D. Eng.:** AGH University of Science and Technology, Academic Centre for Materials and Nanotechnology, Krakow, Poland; **Mirosław Wróbel Ph.D. D.Sc. Eng.:** AGH University of Science and Technology, Faculty of Metal Engineering and Industrial Computer Science, Krakow, Poland; rkowalik@agh.edu.pl

from an indirect-band gap in the thick n-monolayer film to a direct-band gap in the single layers. Among them, molybdenum chalcogenides (MoS_2, $MoSe_2$) have been investigated as electrocatalysts for hydrogen evolution as an alternative to very expensive platinum [1]. Their morphologies and properties are also useful for energy storage applications such as electrodes for Li-ion batteries, supercapacitors [2, 3], and solid lubricants [4]. In addition, the Mo_3Se_4 compound has a remarkable physical property; namely, it is a superconductor with an extremely high upper-critical magnetic field [5].

Usually transition metal chalcogenide compounds can be obtained in thin film form by various methods, including sputtering, chemical bath deposition, selenization, solid state reactions, sulphurization, and electrodeposition [6, 7]. The last one is commonly used as a beneficial technology in producing films and coatings of metals and alloys [8, 9], semiconductors [10–12], and (more specifically) materials used to produce photovoltaic cells [11] or catalysts applied in the hydrogen-production process [13, 14].

An analysis of the electrochemical process of the co-deposition of selenium with molybdenum is interesting in light of the possibilities of Se-Mo alloy deposition [15–20]. Taking into consideration the many existing methods used for obtaining alloy coatings, factors favoring the development of electrochemical methods are the low cost of conducting the process, the ability to coat surfaces of complex shapes, and the possibility for precise control of processes taking place during coatings deposition (i.e., their composition, morphology, structure, and thickness). On the other hand, the electrodeposited coatings are very often amorphous or fine-grained, which is a disadvantage due to the worsened electrical and optical properties. Therefore, the electrodeposited material layers need an additional post-deposition annealing step in a suitable atmosphere in order to improve crystallinity. One other disadvantage of electrodeposition is that it is only possible to apply conducting materials as a substrate.

The electrodeposition of thin films of Mo-Se phases from aqueous baths was studied. The effect of pH on the electrolyte and applied potential were examined. The applied pH and potential of electrolysis were changed systematically in ranges where it significantly effects on the composition of Mo-Se thin films. The composition and structure of the deposited thin films were identified by WD-XRF and XRD techniques. Moreover, the morphology of the samples was analyzed by SEM.

2. Experimental

A conventional three-electrode system was employed, with a platinum foil as a counter electrode (6 cm^2) and a saturated calomel electrode (SCE) as the reference electrode. The substrate for electrodeposition was a copper sheet (2.8 cm^2). The copper sheets were chemically etched in the HNO_3:CH_3COOH:H_3PO_3 1:1:1 mixture for 60 s at a temperature of 60°C before the process of deposition. All chemicals used in this work were of analytical grade. Concentrations of the solutions were 0.002 mM H_2SeO_3 and 0.05 M Na_2MoO_4. The pH of the electrolyte was changed in a range between 2 and 8. The pH was adjusted by

the addition of sulfuric acid or sodium hydroxide. Additionally, sodium sulfate was added to the solution to increase conductivity. The EDAQ EA163 potentiostat was used for the deposition process in the potentiostatic mode. The film growth was carried out for a different time. XRD diffraction patterns were registered with a Rigaku Miniflex II diffractometer with Cu K_a radiation. The morphology of the coatings was studied with the use of scanning electron microscopy (SEM) on an SU 70 instrument (Hitachi). The chemical composition of electrodeposits was characterized by the wavelength-dispersive X-ray fluorescence method (WDXRF) by Rigaku PriMini.

3. Results and discussion

According to thermodynamic predictions, the process of metal chalcogenide synthesis can be achieved when a large excess of less-noble ions is present in the solution [21, 22]. It is the result of the electrochemical properties of selenium compared to the co-deposited metals in aqueous solutions and the free energy of formation of the compounds. According to the Mo-Se binary phase diagram [23], two binary compounds of $MoSe_2$ and Mo_3Se_4 are known to be thermodynamically stable. Proper adjustment of the bath composition should lead to the formation of stoichiometric compounds, and may exclude the presence of an excess of selenium while the solid phase is being formed [24–26]. Consequently, electrolysis was carried out in the solution containing 0.002 M H_2SeO_3 and 0.05 M Na_2MoO_4. Selenium and molybdenum have different ionic forms strongly dependant on the pH of the electrolyte. The chemistry of both elements in aqueous solutions are very well described in the literature [27–29].

Due to the preliminary character of our research, the mechanism for the reduction of selenium and molybdenum were simplified, and the basic forms were used. The process of electrodeposition starts with an initial formation of an Se layer according to the reaction:

$$H_2SeO_3 + 4H^+ + 4e^- \rightarrow Se + 3H_2O \quad (1)$$

The presence of H_2SeO_3 in the electrolyte bath shifts the cathodic current to the region of more positive potential and enables the deposition of molybdenum [29]. The theoretical redox reaction associated with the deposition of Mo can be represented by the reaction [27, 29, 30]:

$$H_2MoO_4 + 6H^+ + 6e^- \rightarrow Mo + 4H_2O \quad (2)$$

When molybdenum atoms are electrodeposited, the formation of chalcogenides could be possible:

$$xMo + ySe \rightarrow Mo_xSe_y \quad (3)$$

It is also important to point out that molybdenum oxide formation is possible according to thermodynamic predictions during electrodeposition [27]. But during the codeposition with other elements (e.g., with Ni), they have a tendency to behave as intermediate and are subsequently reduced to metallic form [31, 32]. It is expected that selenium can play the same role as nickel and "induce" the deposition of molybdenum from an aqueous solution and simultaneously create selenides.

A detailed study was carried out by changing the pH of the electrolyte by a wide range. The deposition time in each case was equal to 15 minutes. It was found that the chemical composition of the Mo-Se films strongly depends on the pH of the solution. Table 1 presents the Mo/Se ratio in the films.

Table 1. Composition of the deposited coatings from electrolyte 0.05 M Na_2MoO_4, 0.002 M H_2SeO_3, 0.1 M Na_2SO_4, T = 55°C at different pH

Deposition potential	Mo/Se % at. ratio					
	pH = 3	pH = 4	pH = 5	pH = 6	pH = 7	pH = 8
–0.3 V	12.40	No deposit	No deposit	–	–	–
–0.4 V	30.81	100 % at. Mo	100 % at. Mo	–	100 % at. Mo	100 % at. Mo
–0.5 V	73.98	46.89	31.84	–	100 % at. Mo	100 % at. Mo
–0.6 V	28.35	49.27	33.59	0.11	100 % at. Mo	100 % at. Mo
–0.7 V	–	–	–	0.61	100 % at. Mo	100 % at. Mo
–0.8 V	–	–	–	1.34	100 % at. Se	100 % at. Mo
–0.9 V	–	–	–	0.55	100 % at. Se	100 % at. Se
–1.0 V	–	–	–	–	7.94	8.42
–1.1 V	–	–	–	–	37.00	100 % at. Mo

Oxygen analysis was not carried out due to limitations of the XRF method. When pH = 2 was applied, very brittle coatings were obtained. This is due to intensive hydrogen evolution and high internal stress appearing in the films (which flaked off during the process of electrolysis, therefore precluding the elemental analysis of the product). The quality of the deposited coatings was improved when the solutions with higher pH values were applied. When solutions with a pH from 3 to 5 were used, the layers were compact and well-adhered to the substrate, but only within the range of potentials from –0.4 to –0.6 V. The coatings were black in color. They consisted mostly of

molybdenum (Tab. 1), even though selenium is more noble and should be deposited first. It can be assumed that, according to the Pourbaix diagram, the molybdenum ions are reduced to the oxides and deposited before selenium [30]:

$$MoO_4^{2-} + 2H_2O + 2e \rightarrow MoO_2 + 4OH^- \quad (4)$$

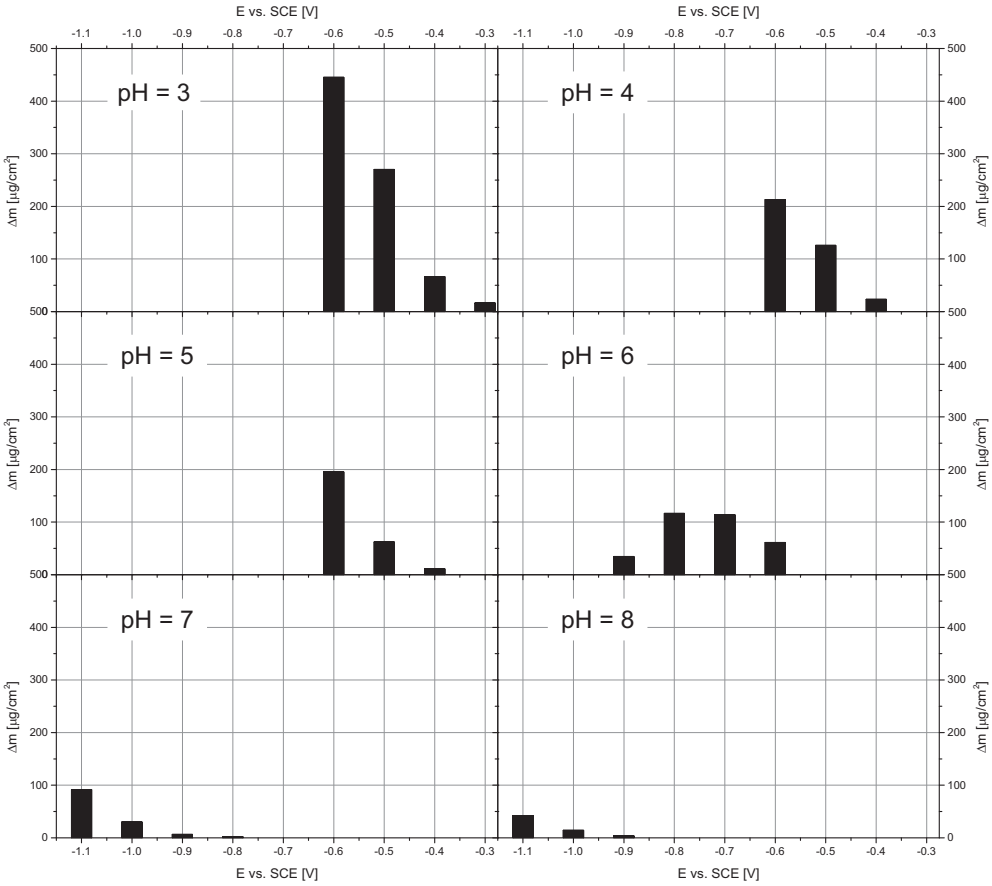

Fig. 1. The mass increase of the electrodes registered after deposition of coatings from electrolyte 0.05 M Na_2MoO_4, 0.002 M H_2SeO_3, 0.1 M Na_2SO_4, T = 55°C at different pH

The X-ray diffraction studies did not reveal any crystalline phases except copper substrate, so the presence of oxides was not confirmed. These results indicate that the obtained films were amorphous. Appling more-negative potentials caused the flaking off of the films from the electrode, similarly when an electrolyte with pH = 2 was used. The mass increment of the electrodes (Fig. 1) indicates that the rate of deposition was very fast and can be responsible for the appearance of internal stress in the deposits as

well as its brittleness. Additionally, the process of hydrogen evolution was very intense when the acid pH and very-negative potentials were applied. These effects negatively impacted the quality of the deposits.

When a bath of pH = 6 was applied, the composition of the films changed significantly (Tab. 1). The higher content of selenium in the deposit was detected compared to the layers obtained at the same range of potentials but at a lower pH. The ratio between elements in the deposits is very close to the stoichiometry of molybdenum chalcogenides.

The further increasing of pH limits the possibility of deposition of Mo-Se coatings. There was no deposit when a more-positive potential than E = −0.7 V (in the case of pH = 7 and then E = −0.8 V at pH = 8) were applied. Below potential −0.7 V, an increment of the mass of the electrode was detected. The obtained films were very thin due to the low rate of chalcogenide deposition in the neutral and weak-alkaline pHs [10]. The films were composed mostly of selenium when more-positive potentials were applied, or in the majority of molybdenum in the case of applying more-negative potentials. There were no layers with intermediate composition close to the stoichiometry of molybdenum chalcogenides.

In order to determine the influence of deposition time on film composition, electrodeposition was performed by varying the deposition time from 5 to 60 minutes. The processes of electrolysis were conducted in the electrolyte at pH = 6 and at potential −0.8 V vs. SCE. The mass of the deposits increases with the time of electrolysis (Fig. 2), and all of the coatings were homogenous and well-adherent to the substrate. It is a very important issue that the coatings are compact and do not flake off when their thickness increases. The composition of the films slightly changed by decreasing molybdenum content in the range of 10% at. (Tab. 2). It is suggested that the mechanism of the co-reduction of molybdenum and selenium is not disturbed by the growth of semiconducting layers.

Table 2. Composition of the deposited coatings from electrolyte 0.05 M Na_2MoO_4, 0.002 M H_2SeO_3, 0.1 M Na_2SO_4, T = 55°C at different time of deposition

Time of deposition, [s]	**Mo/Se % at. ratio**
300	1.47
600	1.42
900	1.41
1800	0.93
3600	1.15

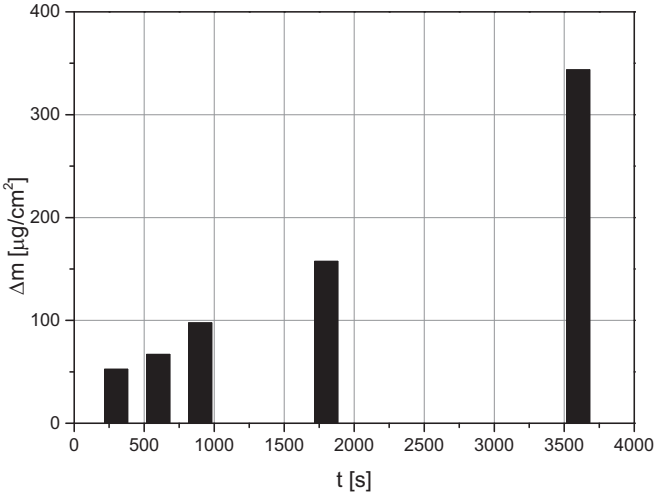

Fig. 2. The mass increment of the samples after deposition from electrolyte 0.05 M Na_2MoO_4, 0.002 M H_2SeO_3, 0.1 M Na_2SO_4, T = 55°C at different time of deposition

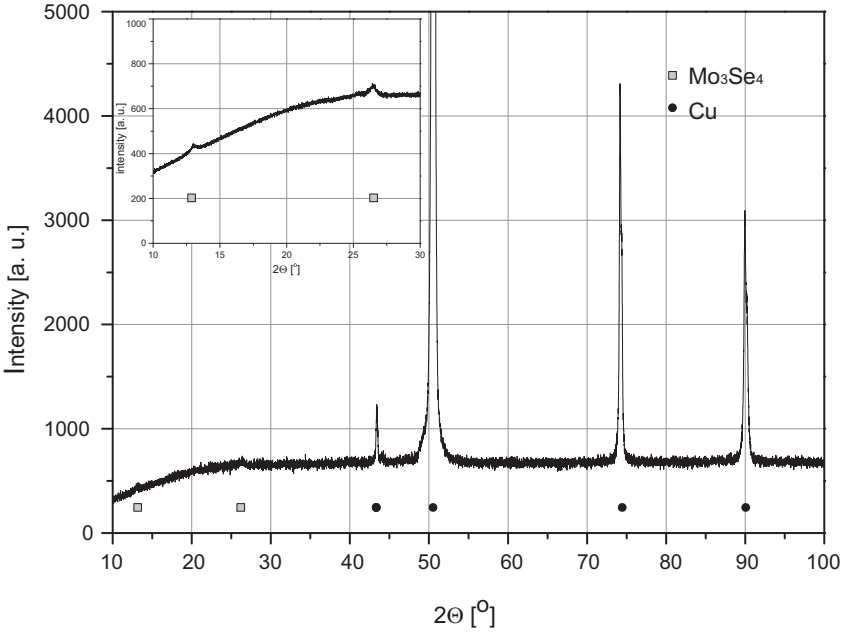

Fig. 3. XRD patterns of Mo-Se coatings deposited from electrolyte: 0.05 M Na_2MoO_4, 0.002 M H_2SeO_3, 0.1 M Na_2SO_4, pH = 6, T = 55°C, at potential –0.6 V vs. SCE

The selected X-ray diffraction (XRD) pattern of the electrodeposited coating on a copper substrate is shown in Figure 3. The phase analysis of the coatings was hindered.

The diffractogram mostly exhibits peaks related to the copper substrate (and only two very small peaks associated with the Mo_3Se_4 phase). This is due to the amorphous structure of the deposits [12]. This effect is characteristic for coatings obtained in the limiting current regime [24].

The surface morphology of Mo-Se thin films deposited at potential –0.6 V vs. SCE on copper substrate is shown in Figure 4. The as-deposited films have a homogenous and compact layer structure with no visible grain structure. It covers the copper substrate well without any cracks or pinholes. The characteristic flake-like structure is visible when a higher magnification is applied.

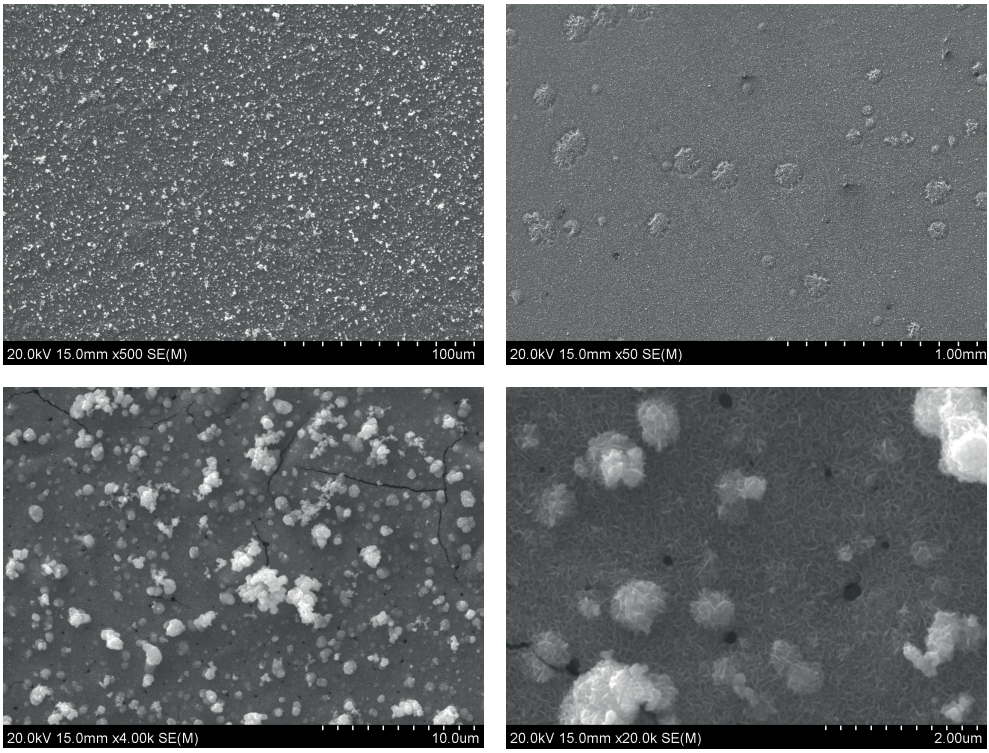

Fig. 4. The surface morphology of deposited layers obtained using Cu substrate. Bath composition: 0.05 M Na_2MoO_4, 0.002 M H_2SeO_3, pH = 6, T = 55°C, at potential –0.6 V vs. SCE

4. Summary

It has been demonstrated that co-deposition of molybdenum and selenium is possible from a simple bath without the addition of any complex agents. The proper adjustment of the process of electrolysis has a crucial influence on the composition of the deposited

films, and the very important factor is the pH of the electrolyte. When a pH below 6 is applied, the coatings consist mostly of molybdenum. Moreover, the coatings were very brittle when deposited at pH 2. The deposition of the coatings is possible at potentials below –0,8 V (when pH increased above 6), but the coatings consist mostly of pure selenium or molybdenum.

Synthesis of the films with a stoichiometry close to the molybdenum chalcogenides is limited to pH = 6 and is possible in a wide range of potentials (from –0.6 to –0.9 V). The obtained films characterize the amorphous structure and impede phase analysis. In consequence, further work is required that embraces a more-detailed phase analysis by XPS and conformation of the presence of selenide compounds or oxides (which is currently in progress in our laboratory).

Acknowledgments

This work was supported by the Polish National Science Center under grant 2011/01/D/ST5/05743. K. Mech gratefully acknowledges the financial support of the Foundation for Polish Science within the Start scholarship (072.2014).

References

[1] Yang J., Shin H.S.: Recent advances in layered transition metal dichalcogenides for hydrogen evolution reaction. Journal of Materials Chemistry A, 2, 17 (2014), 5979–5985

[2] Pumera M., Sofer Z., Ambrosi A.: Layered transition metal dichalcogenides for electrochemical energy generation and storage. Journal of Materials Chemistry A, 2, 24 (2014), 8981–8987

[3] Chan K., Tsai C., Hansen H. A., Nørskov J. K.: Molybdenum sulfides and selenides as possible electrocatalysts for CO_2 reduction. Chemcatchem, 6, 7 (2014), 1899–1905

[4] Ponomarev E.A., Neumann-Spallart M., Hodes G., Lévy-Clément C.: Electrochemical deposition of MoS_2 thin films by reduction of tetrathiomolybdate. Thin Solid Films, 280, 1–2 (1996), 86–89

[5] Le Berre F., Tshimanga D., Guilloux A.L., Leclercq J., Sergent M., Peña O., Horyn R., Wojakowski A.: Rare-earth doping of the Mo_3Se_4 superconductor. Physica B: Condensed Matter, 228, 3–4 (1996), 261–271

[6] Aruchamy A.: Photoelectrochemistry and photovoltaics of layered semiconductors. Kluwer Academic, Dordrecht – Boston, 1992.

[7] Shariza S., Anand T.J.S.: Effect of deposition time on the structural and optical properties of molybdenum chalcogenides thin films. Chalcogenide Letters, 8, 9 (2011), 529–539

[8] Landolt D.: Electrodeposition science and technology in the last quarter of the twentieth century. Journal of the Electrochemical Society, 149, 3 (2002), S9–S20

[9] Mech K., Żabiński P., Mucha M., Kowalik R.: Electrodeposition of catalytically active Ni-Mo alloys. Archives of Metallurgy and Materials, 58, 1 (2013), 227–229

[10] Rajeshwar K.: Electrosynthesized thin films of group II–VI compound semiconductors, alloys and superstructures. Advanced Materials, 4, 1 (1992), 23–29

[11] Lincot D.: Electrodeposition of semiconductors. Thin Solid Films, 487, 1–2 (2005), 40–48

[12] Kowalik R., Zabiński P., Fitzner K.: Electrodeposition of ZnSe. Electrochimica Acta, 53, 21 (2008), 6184–6190

[13] Alkire R.C.: Advances in Electrochemical Science and Engineering, vol. 12. Wiley-VCH, Chichester, 2010
[14] Zabiński P., Mech K., Kowalik R.: Co-Mo and Co-Mo-C alloys deposited in a magnetic field of high intensity and their electrocatalytic properties. Archives of Metallurgy and Materials, 57, 1 (2012), 127–133
[15] Chandra S., Sahu S.N.: Electrodeposited semiconducting molybdenum selenide films. I. Preparatory technique and structural characterisation. Journal of Physics D: Applied Physics, 17, 10 (1984), 2115–2123
[16] Joseph Sahaya Anand T., Sanjeeviraja C., Jayachandran M.: Preparation of layered semiconductor ($MoSe_2$) by electrosynthesis. Vacuum, 60, 4 (2000), 431–435
[17] Dukstiene N., Kazancev K., Prosicevas I., Guobiene A.: Electrodeposition of Mo-Se thin films from a sulfamatic electrolyte. Journal of Solid State Electrochemistry, 8, 5 (2004), 330–336
[18] Delphine S.M., Jayachandran M., Sanjeeviraja C.: Pulsed electrodeposition and characterization of molybdenum diselenide thin film. Materials Research Bulletin, 40, 1 (2005), 135–147
[19] Dukstiene N., Tatariskinaite L.: Electrochemical examination of the influence of H_2SeO_3 on molybdenum electrodeposition on tin oxide electrode from aqueous citrate electrolyte. Polish Journal of Chemistry, 80, 10 (2006), 1715–1729
[20] Hahn B.P., Stevenson K.J.: Cathodic electrodeposition of mixed molybdenum-selenium oxides. Journal of Electroanalytical Chemistry, 638, 1 (2010), 151–160
[21] Kröger F.A.: Cathodic deposition and characterization of metallic or semiconducting binary alloys or compounds. Journal of the Electrochemical Society, 125, 12 (1978), 2028–2034
[22] Gawęda S., Kowalik R., Kwolek P., Macyk W., Mech J., Oszajca M., Podborska A., Szaciłowski K.: Nanoscale digital devices based on the photoelectrochemical photocurrent switching effect: Preparation, properties and applications. Israel Journal of Chemistry, 51 (2011), 36–55
[23] Baker H.: Alloy phase diagrams. Materials Park, Ohio, ASM International, 1992
[24] Kowalik R., Fitzner K.: About the conditions of zinc selenide electrodeposition from aqueous solutions. Metallurgy and Foundry Engineering, 30, 2 (2004), 140–141
[25] Kowalik R., Fitzner K.: Analysis of the mechanism for electrodeposition of the ZnSe phase on Cu substrate. Journal of Electroanalytical Chemistry, 633, 1 (2009), 78–84
[26] Kowalik R., Szaciłowski K., Zabiński P.: Photoelectrochemical study of ZnSe electrodeposition on Cu electrode. Journal of Electroanalytical Chemistry, 674 (2012), 108–112
[27] Pourbaix M.: Atlas of Electrochemical Equilibria in Aqueous Solutions. Pergamon, New York, 1966
[28] Pope M.T.: Heteropoly and isopoly oxometalates. Springer-Verlag, Berlin – New York, 1983
[29] Bouroushian M.: Electrochemistry of metal chalcogenides. Springer, Berlin, 2010
[30] Nuñez M.: Metal electrodeposition. Nova Science Publishers, New York, 2005
[31] Podlaha E.J., Landolt D.: Induced codeposition. III. Molybdenum alloys with nickel, cobalt, and iron. Journal of the Electrochemical Society, 144, 5 (1997), 1672–1680
[32] Podlaha E.J., Landolt D.: Induced codeposition: I. An experimental investigation of Ni-Mo alloys. Journal of the Electrochemical Society, 143, 3 (1996), 885–892